Bioactive Materials 65 (2026) 644–662

Contents lists available at ScienceDirect

Bioactive Materials

journal homepage: www.keaipublishing.com/en/journals/bioactive-materials

Growth plate cartilage-targeting nanoparticles for pharmacological treatment of hypochondroplasia

Shang-Hui Ye [a,c,1], Lian-Jie Li [a,c,1], Yi-Jiao Wang [e,f,1], Cheng-Run Yuan [e,1], Jie Han [a,c], Dan He [e], Lin Che [h,i], Xiao-Hui Chen [a], Rong Shen [c], Jian Yang [j], Matthew B. Greenblatt [k,l], Xian-Xian Yang [m,*], Jian-Min Huang [g,**], Jing Chen [e,f,***], Ren Xu [a,b,c,d,****]

[a] The First Affiliated Hospital of Xiamen University-ICMRS Collaborating Center for Skeletal Stem Cells, Faculty of Medicine and Life Sciences, School of Medicine, Xiamen University, Xiamen, 361102, China
[b] Beijing Research Institute of Traumatology and Orthopaedics, National Centre for Orthopaedics, Beijing Jishuitan Hospital, Beijing, 100035, China
[c] Fujian Provincial Key Laboratory of Organ and Tissue Regeneration, School of Medicine, Xiamen University, Xiamen, 361102, China
[d] State Key Laboratory of Vaccines for Infectious Diseases, Xiang An Biomedicine Laboratory, Xiamen University, Xiamen, 361102, China
[e] Department of Child Health, Department of Pediatrics, Women and Children's Hospital, School of Medicine, Xiamen University, Xiamen, 361102, China
[f] School of Life Sciences, Xiamen University, Xiamen, 361102, China
[g] Department of Orthopedics, Chenggong Hospital (73rd) affiliated to Xiamen University, Xiamen, 361000, China
[h] State Key Laboratory of Oncology in South China, Sun Yat-sen University Cancer Center, Guangzhou, 510060, China
[i] Guangzhou National Laboratory, Guangzhou, 510005, China
[j] Department of Materials Science and Engineering, Westlake University, Hangzhou, 310030, China
[k] Department of Pathology and Laboratory Medicine, Weill Cornell Medicine, New York, NY, 10065, USA
[l] Skeletal Health and Orthopedic Research Program, Hospital for Special Surgery, New York, NY, 10065, USA
[m] Department of Plastic and Reconstructive Surgery, Shanghai Ninth People's Hospital, Shanghai Jiao Tong University School of Medicine, Shanghai, 200011, China

ARTICLE INFO

Keywords:
Hypochondroplasia
Chondrocyte membranes
Growth plate cartilage
Drug delivery
Hedgehog signaling pathway

ABSTRACT

Hypochondroplasia (HCH) is a systemic cartilage disorder caused by gain-of-function mutations in *FGFR3*, resulting in overactivation of signaling and short stature. Pharmacological therapy remains the primary treatment but provides only partial symptomatic relief, as the avascular and alymphatic nature of growth plate cartilage severely limits drug delivery and accumulation. To address this challenge, we developed CT-CM-NPs, a drug delivery system coated with primary chondrocyte membranes and further modified with the collagen II-binding peptide WYRGRL. This design retains the inherent biological properties of native membranes while incorporating targeting capability, enabling efficient cartilage targeting and penetration. In vivo, CT-CM-NPs effectively delivered the Hedgehog pathway agonist Purmorphamine to the growth plate cartilage in an HCH mouse model, resulting in upregulated Hedgehog signaling, restored impaired ciliogenesis, improved chondrocyte phenotypes, and ultimately increased bone and body length. Collectively, these findings establish CT-CM-NPs as a promising and potentially translatable nanoplatform for the treatment of HCH.

Peer review under the responsibility of editorial board of Bioactive Materials.

* Corresponding authors. Department of Plastic and Reconstructive Surgery, Shanghai Ninth People's Hospital, Shanghai Jiao Tong University School of Medicine, Shanghai, 200011, China.

** Corresponding author. Department of Orthopedics, Chenggong Hospital (73rd) affiliated to Xiamen University, Xiamen, 361000, China.

*** Corresponding author. Department of Child Health, Department of Pediatrics, Women and Children's Hospital, School of Medicine, Xiamen University, Xiamen, 361102, China.

**** Corresponding author. The First Affiliated Hospital of Xiamen University-ICMRS Collaborating Center for Skeletal Stem Cells, Faculty of Medicine and Life Sciences, School of Medicine, Xiamen University, Xiamen, 361102, China.

E-mail addresses: yangxx112042@sh9hospital.org.cn (X.-X. Yang), hjm0505@xmu.edu.cn (J.-M. Huang), chenjing8469899@126.com (J. Chen), xuren526@xmu.edu.cn (R. Xu).

[1] These authors contributed equally to this work.

https://doi.org/10.1016/j.bioactmat.2026.06.018
Received 12 March 2026; Received in revised form 27 May 2026; Accepted 12 June 2026

1. Introduction

Systemic cartilage disorders are a group of diseases caused by multiple factors, including genetic defects, metabolic abnormalities, and immune dysregulation [1–3]. The pathological characteristics are marked by widespread involvement of cartilage tissues, leading to cartilage developmental abnormalities, imbalance in tissue homeostasis, and functional disturbances [3,4]. Unlike localized cartilage lesions, systemic cartilage disorders involve extensive tissue abnormalities, making localized surgical interventions less effective. Currently, systemic drug therapy remains the primary treatment strategy in clinical practice [5,6].

Hypochondroplasia (HCH) is a representative genetic systemic cartilage disorder, primarily caused by mutations in the fibroblast growth factor receptor 3 (*FGFR3*) gene, with an incidence comparable to achondroplasia (ACH), affecting approximately 1 in 15,000 individuals [7,8]. The main clinical manifestation is short stature. To date, the treatment of HCH primarily relies on pharmacological therapy, with long-term use of growth hormone being a common treatment approach [9,10]. However, the lack of target specificity in growth hormone therapy often leads to systemic side effects, such as hyperglycemia and hyperlipidemia [11]. Recently, C-type natriuretic peptide (CNP) analogs, such as Vosoritide, have shown promising results in clinical trials for ACH [12,13]. Yet its impact on final height, as well as on spinal and cranial abnormalities, remains inadequately evaluated [14]. Moreover, the long-term use of these protein-based drugs is constrained by both high costs and the risk of immune resistance. Small-molecule drugs, with their inherently low immunogenicity and lower manufacturing costs, have therefore emerged as an attractive alternative for sustained therapy. Among these, agents targeting the Hedgehog pathway have shown therapeutic promise [15,16]. However, their clinical translation is hindered by off-target effects and the inherent challenges posed by the avascular and alymphatic nature of growth plate cartilage. These limitations underscore the urgent need for novel therapeutic strategies that integrate both cartilage-targeting and matrix-penetrating capabilities to enable safe and effective treatment for HCH.

Cell membrane biomimetic technology has attracted considerable attention for its ability to combine circulation stability with low immunogenicity [17,18]. These properties have enabled the systemic delivery of small-molecule and nucleic acid therapeutics, even achieving traversal of stringent barriers such as the blood-brain and maternal-fetal barriers [19,20]. Building on this foundation, secondary membrane engineering further introduces targeting capabilities, thereby enhancing safety while maintaining therapeutic efficacy and improving translational potential [21]. Initial platforms primarily employed circulating cell types such as leukocytes, platelets, and other immune cells because of their inherent trafficking behavior [22,23]. As the field progressed, membrane sources expanded to tissue-resident cells, including tumor cells and astrocytes, to harness their specialized microenvironmental interactions [24–26]. Despite the central role of bone in the musculoskeletal system, biomimetic delivery platforms derived from resident cells remain rare. Chondrocytes have recently emerged as promising candidates for intra-articular delivery due to their intrinsic interactions with cartilage matrix components [27,28]. However, their tissue-resident nature still greatly limits their applicability in systemic delivery. Even so, the unique niche and distinctive extracellular interactions of chondrocytes suggest an underexplored potential for targeted cartilage delivery.

Herein, we developed a biomimetic drug-delivery system, termed CT-CM-NPs, by integrating chondrocyte-derived cell membranes with the collagen II-binding peptide WYRGRL (Trp-Tyr-Arg-Gly-Arg-Leu) [29,30]. This hybrid system demonstrates excellent biocompatibility, preserving the interactions between chondrocytes and the extracellular matrix. Targeting modifications further enhance its specificity while reducing circulation time to improve safety. Notably, it exhibits remarkable growth plate cartilage-targeting capabilities, as confirmed by both in vitro and in vivo experiments. In MTS and explant cultures, it further demonstrated efficient penetration into and sustained retention within cartilage tissue. Using this system, systemic delivery of Purmorphamine (PM), a Hedgehog pathway agonist, was achieved throughout adolescence in HCH mice, effectively rescuing defective ciliogenesis, promoting cartilage regeneration, and ultimately reversing abnormalities in bone and body length (Fig. 1). Together, these findings establish a promising and potentially translatable nanoplatform for the treatment of HCH and provide a new strategy for addressing systemic cartilage disorders.

2. Materials and methods

2.1. Materials

Dulbecco's Modified Eagle Medium (DMEM, 11965092), fetal bovine serum (FBS, A5669701), Penicillin/Streptomycin (15140122), and phosphate-buffered saline (PBS, 10010023) were obtained from Gibco (USA). Methyl cellulose (9004-67-5), DiR (HY-D1048), Collagen alpha-1 (II) chain/COL2A1 protein (Human, HY-P75333), Rottlerin (HY-18980), Nystatin (HY-17409), Dynasore (HY-15304), Cytochalasin D (HY-N6682) and sodium heparin (9041-08-1) were obtained from MedChemExpress (MCE, USA). Trypsin solution (0.25%) was purchased from Biosharp (China). Dimethyl sulfoxide (DMSO, 67-68-5), phenylmethylsulfonyl fluoride (PMSF, 329-98-6), and anti-acetylated tubulin antibody (T7451) were obtained from Sigma-Aldrich (USA). RIPA lysis buffer (89900), TNF-α ELISA kit (Mouse, 88-7324), IL-6 ELISA kit (Mouse, 88-7064), anti-IHH antibody (H00003549-M05), and fluorescent secondary antibodies, including donkey anti-rabbit IgG (H&L) Alexa Fluor 488 (2072687), donkey anti-rat IgG (H&L) Alexa Fluor 488 (2092264), and goat anti-rabbit IgG (H&L) Alexa Fluor 594 (2201598) were purchased from Invitrogen (USA). Integrin β1 (D2E5) Rabbit mAb (9699S), N-Cadherin (D4R1H) XP® Rabbit mAb (13116S), E-Cadherin (24E10) Rabbit mAb (3195S), CD44 (156-3C11) Mouse mAb (3570T) Na, K-ATPase Rabbit mAb (#3010), Integrin alpha5 Rabbit mAb (#4705) and Gli1 (L42B10) Mouse mAb (#2643) were obtained from Cell Signaling Technology (USA). Confocal microscopy dishes was obtained from NEST (20 mm, 801001, China). Type II collagenase (LS004202) was from Worthington Biochemical Corporation. (USA). FITC-Phalloidin (R32267-300T) were obtained from Shanghai Yuanye Bio-Technology Co., Ltd. (China). 4′,6-Diamidino-2-phenylindole dihydrochloride (DAPI, 28718-90-3), Cell Counting Kit-8 (CCK-8, AC10873), and Purmorphamine (PM, 483367-10-8) were purchased from Acmec Biochemical Co., Ltd. (China). Anti-Integrin Alpha 1/ITGA1 Antibody (BA1731) and anti-Integrin Alpha 3/ITGA3 Antibody (A02902) was obtained from BOSTER (China). DiO (G1704), Triton X-100 (9002-93-1), Safranin O (477-73-6), and Fast Green FCF (2353-45-9) were obtained from Solarbio (Beijing, China). Acid Red 87 staining solution (ZLI-9613), and Hematoxylin staining solution (ZLI-9610) were obtained from ZSBio (Beijing, China). The cartilage-targeting peptide WYRGRL (Trp-Tyr-Arg-Gly-Arg-Leu, >98% purity, confirmed by HPLC) was synthesized by Wansheng Haotian Biotechnology Co., Ltd. (Shanghai, China). DSPE-PEG_{2k}-NHS (1,2-distearoyl-sn-glycero-3-phosphoethanolamine-N-[methoxy (polyethylene glycol)-2000]-N-hydroxysuccinimide, >98% purity, confirmed by HPLC) and poly (lactic-co-glycolic acid) (PLGA) were synthesized by Xi'an Ruixi Biological Technology Co., Ltd. (Xi'an, China). All other organic solvents and reagents, including isopropanol, ethanol, and xylene, were obtained from Sinopharm Chemical Reagent Co., Ltd. (China), unless otherwise specified.

2.2. Cell culture

Primary chondrocytes were isolated from the femoral condyles and tibial plateaus of 6 or 7-day-old C57BL/6 mice. Briefly, articular cartilage was carefully dissected, minced into 1-5 mm^3 fragments, and

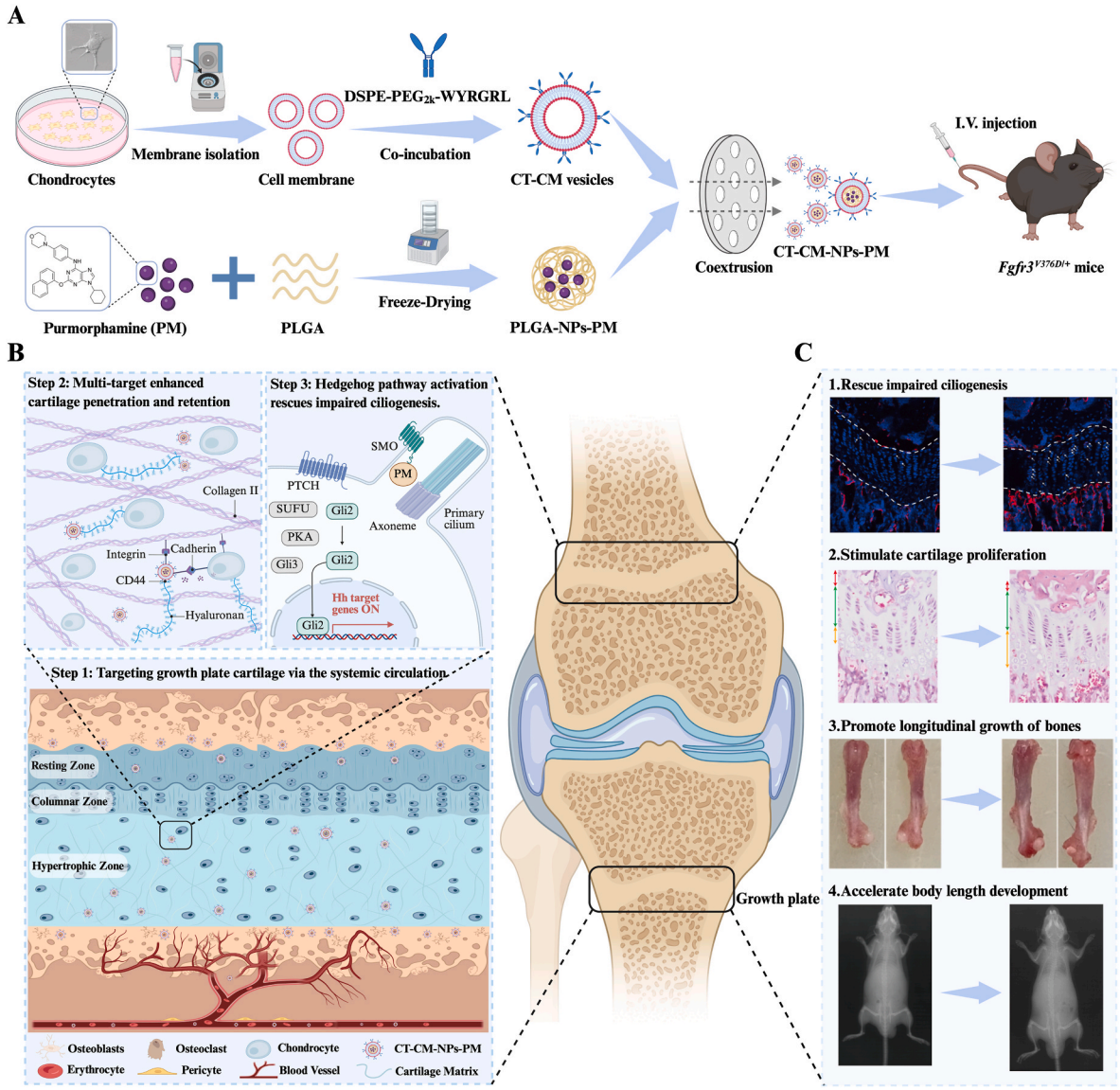

Fig. 1. Schematic illustration of CT-CM-NPs-PM for the treatment of HCH. (A) Preparation process of CT-CM-NPs-PM. (B) Proposed therapeutic mechanism of CT-CM-NPs-PM: 1) WYRGRL-mediated binding to COL II enables targeted homing to growth plate cartilage; 2) Chondrocyte membrane coating enhances cartilage retention and penetration through interactions with chondrocytes and the extracellular matrix; 3) PM activates SMO and stimulates Hedgehog signaling, thereby restoring impaired ciliogenesis. (C) CT-CM-NPs-PM restores impaired ciliogenesis, improves chondrocyte phenotypes, and ultimately promotes bone elongation and body growth in HCH.

digested with 0.2% type II collagenase in a shaking incubator at 37 °C for 4-6 h. The resulting cell suspension was filtered through a sterile 70 μm cell strainer to remove undigested tissue. After centrifugation and three washes with PBS, the isolated chondrocytes were resuspended and cultured in complete DMEM medium (DMEM, 10% FBS, and 1% Penicillin/Streptomycin). Cells were maintained under sterile conditions at 37 °C in a humidified incubator with 5% CO_2. ATDC-5 and RAW264.7 cells were obtained from iCell Bioscience Inc (Shanghai, China) cultured with complete DMEM medium and incubated at 37 °C in a 5% CO_2 incubator.

2.3. Animal use and care

Fgfr3$^{V376D/+}$ mice were produced as previously described [31]. Mice were housed, bred in a barrier facility, fed ad libitum chow, and followed a standard day-night lighting cycle.

2.4. Synthesis of the DSPE-PEG$_{2k}$-WYRGRL

The cartilage-targeting peptide WYRGRL and DSPE-PEG$_{2k}$-NHS were individually dissolved in 5 mM HEPES buffer at 1 mg/mL. The two components were then mixed at a 1:1 M ratio and allowed to react at room temperature for 24 h to synthesize DSPE-PEG$_{2k}$-WYRGRL. The reaction mixture was dialyzed against distilled water using a dialysis bag (molecular weight cutoff of 3000 Da) for 48 h. Finally, the dialyzed solution was freeze-dried and stored at −20 °C.

2.5. Surface plasmon resonance (SPR) analysis of DSPE-PEG$_{2k}$-WYRGRL binding to hCOL2A1

The binding affinity of DSPE-PEG2k-WYRGRL toward human type II collagen α1 chain (hCOL2A1) was evaluated using a Biacore 8K SPR system (Cytiva) equipped with a CM5 sensor chip. The sensor surface was activated with a freshly prepared 1:1 mixture of 400 mM N-ethyl-N′-(3-dimethylaminopropyl) carbodiimide (EDC) and 100 mM N-

hydroxysuccinimide (NHS) at a flow rate of 10 μL/min for 420 s. Recombinant hCOL2A1 (20 μg/mL) was immobilized onto the sample flow cell (Fc2) to an immobilization level of approximately 12,600 RU, while the reference flow cell (Fc1) was left unmodified. Remaining activated groups were blocked with 1 M ethanolamine hydrochloride (pH 8.5) at 10 μL/min for 420 s.

For kinetic analysis, DSPE-PEG2k-WYRGRL was diluted in running buffer (PBS containing 0.05% Tween-20) to concentrations ranging from 0.31 to 20.00 μM (0.31, 0.63, 1.25, 2.50, 5.00, 10.00, and 20.00 μM). Samples were injected sequentially over both flow cells at a flow rate of 20 μL/min, with an association phase of 100 s followed by a dissociation phase of 180 s. Regeneration was performed after each cycle to restore baseline conditions.

Sensorgrams were double-reference corrected and analyzed using Biacore Insight Evaluation Software (Cytiva). Binding kinetics were determined by fitting the data to a 1:1 Langmuir binding model, and the equilibrium dissociation constant (K_D) was calculated accordingly.

2.6. Isolation of primary chondrocyte plasma membranes

To isolate plasma membranes from primary chondrocytes, passage 1 (P1) chondrocytes were first washed with PBS, gently scraped, and collected by centrifugation at 1500 rpm for 5 min. The cell membranes were then extracted using a multistep differential centrifugation protocol (2000 rpm for 10 min, 5000 rpm for 10 min, and 15,000 rpm for 60 min), following sonication [32]. The collected membrane fraction was resuspended in physiological saline and quantified using the BCA (Pierce BCA Protein Assay Kit; Thermo). The final chondrocyte plasma membrane preparation was stored at −80 °C until use.

2.7. Isolation of red blood cell (RBC) plasma membranes

To isolate RBC plasma membranes, whole blood was collected from C57BL/6 mice. The blood was washed three times with PBS to remove serum, followed by centrifugation at 5000 rpm for 5 min. The washed RBCs were then resuspended in hypotonic (0.25×) PBS on ice to induce membrane lysis. The cell lysate was centrifuged at 15,000 rpm for 20 min to remove hemoglobin. This lysis and centrifugation process was repeated until the supernatant became clear, indicating effective hemoglobin removal. The final RBC membranes were quantified using a BCA assay and stored in physiological saline at −80 °C for future use.

2.8. Synthesis of PLGA-NPs-PM

PLGA nanoparticles loaded with PM were prepared using the microemulsion method. Briefly, 25 mg of PLGA and 2.5 mg of purmorphamine were dissolved in 1 mL of DMSO, followed by the addition of 2 mL of deionized water containing 1% PVA. The resulting mixture was emulsified by probe ultrasonication in an ice-water bath for 10 min using a 1-s on/2-s off pulse cycle. The emulsion was then centrifuged at 15,000 rpm for 30 min. The nanoparticles were washed three times with deionized water, freeze-dried, and stored at −20 °C until use. To determine the amount of encapsulated PM, 1 mg of lyophilized PLGA-NPs-PM was dissolved in 1 mL of DMSO to completely disrupt the nanoparticle structure and release the encapsulated drug. Subsequently, 200 μL of the solution was transferred to a 96-well plate, and fluorescence intensity was measured at 315 nm. The PM content was quantified using a standard calibration curve and used for subsequent determination of encapsulation efficiency and drug loading capacity.

2.9. Preparation and characterization of CT-CM-NPs-PM

To prepare membrane-coated nanoparticles, RM vesicles, CM vesicles, or CT-CM vesicles (80 μL, corresponding to 0.4 mg membrane protein) were mixed with 200 μL of PLGA-NPs-PM suspension (corresponding to 1.2 mg nanoparticles). The mixture was extruded through a 400 nm polycarbonate membrane using a mini extruder for 20 cycles to facilitate membrane coating. Excess unbound membrane was removed by centrifugation at 15,000 rpm for 20 min. The resulting membrane-coated nanoparticles (CM-NPs-PM, RM-NPs-PM, and CT-CM-NPs-PM) were resuspended in physiological saline for subsequent use. Membrane coating efficiency (MCE, %) was quantified using the BCA assay. At a PLGA-to-membrane protein weight ratio of 3:1, the coating efficiency reached approximately 90%. The physical characteristics of the nanoparticles were evaluated using transmission electron microscopy (TEM; Tecnai G2 Spirit BioTwin, Tools for NanoTech, FEI), dynamic light scattering (DLS; Zetasizer Nano ZS-90, Malvern Instruments), and zeta potential analysis (Zetasizer Nano ZS-90, Malvern Instruments).

2.10. In vitro cellular uptake of nanoparticles

Cellular uptake was evaluated using flow cytometry and confocal laser scanning microscopy (CLSM). Primary chondrocytes and RAW264.7 cells were seeded into observation dishes at a density of 1×10^4 cells per dish. Once the cells reached approximately 80% confluence, the medium was replaced with DMEM containing DiR-labeled PLGA-NPs, RM-NPs, CM-NPs, or CT-CM-NPs, followed by incubation at 37 °C for 1 or 4 h. After incubation, the supernatant was removed, and the cells were collected. A total of 1×10^5 cells were then analyzed by flow cytometry (Attune NxT; Thermo Fisher Scientific, USA). The data were analyzed using FlowJo (v.10.8.1). For CLSM, chondrocytes were gently washed three times with PBS and fixed with 4% paraformaldehyde for 10 min, followed by another three PBS washes. Subsequently, the cells were stained with FITC-phalloidin for 30 min and washed three times with PBS. Finally, the nuclei were stained with DAPI for 30 min, followed by an additional three PBS washes. Fluorescence images were acquired using a confocal microscope as described [33] (Leica TCS SP8 DLS; Leica Microsystems).

2.11. Flow cytometry analysis of endocytosis pathways

To investigate the cellular internalization pathways of nanoparticles, primary mouse chondrocytes were seeded in 6-well plates at a density of 1×10^4 cells per well and cultured overnight until reaching approximately 80% confluence. Cells were then pretreated with dynasore (40 μM), nystatin (54 μM), cytochalasin D (10 μM), or rottlerin (2 μM) for 30 min at 37 °C. Subsequently, DiR-labeled CM-NPs or CT-CM-NPs were added at a final concentration of 100 μg/mL and incubated with the cells for an additional 2 h. Following incubation, cells were washed thoroughly with PBS, harvested, and analyzed by flow cytometry. A total of 1×10^5 cells were collected for each sample, and the percentage and fluorescence intensity of DiR-positive cells were quantified. Flow cytometry data were analyzed using FlowJo software (v10.8.1) [27].

2.12. RT-qPCR analysis

Total RNA was extracted using the Trizol reagent (Vazyme, R401-01), and reverse transcription was performed with the HiScript II Q RT SuperMix (Vazyme, R223-01). Quantitative PCR was carried out with the ChamQ Universal SYBR qPCR Master Mix (Vazyme, Q711-02) on a QuantStudio 1 system (Applied Biosystems, Thermo Fisher Scientific, USA). Gene expression levels were determined using the comparative cycle threshold (Ct) method, with HPRT serving as the internal control. Relative expression was calculated using the $2^{-\Delta\Delta Ct}$ method. The specific primers designed from mouse sequences for SYBR Green detection are listed in Supporting Information (Table S1).

2.13. Western blotting

As described previously, membranes from primary chondrocytes were lysed, mixed with SDS sample buffer, and heated at 95 °C for 5 min. Equal amounts of protein were separated by SDS-PAGE (Sangon Biotech,

151-21-3) and transferred onto PVDF membranes (Millipore, IPVH00010). The membranes were blocked with 5% nonfat milk and incubated with primary antibodies overnight at 4 °C. After washing, membranes were incubated with the appropriate secondary antibodies, and immunoreactive bands were detected by enhanced chemiluminescence.

2.14. In vivo biodistribution of nanoparticles

Each mouse received a single intravenous injection of DiR-labeled PLGA-NPs, RM-NPs, CM-NPs, or CT-CM-NPs at a dose of 100 μg. For in vivo biodistribution analysis, fluorescence imaging of the hind limbs was performed using the IVIS Spectrum (PerkinElmer, USA) at 8, 16, 24, 48, and 72 h post-injection. For ex vivo biodistribution analysis, independent cohorts of mice were sacrificed at the corresponding time points following a single administration. Major organs, including the heart, lungs, liver, spleen, kidneys, and femurs, were harvested for fluorescence imaging. In particular, distal femoral regions from both hind limbs were collected and analyzed to evaluate nanoparticle accumulation within the growth plate.

2.15. Frozen sections of hard tissue

Following treatment with different nanoparticle formulations, femurs were harvested from mice, fixed for 24 h, and washed with PBS. Samples were then embedded in OCT compound (Sakura, 4582) and frozen at −80 °C for 24 h. Prior to sectioning, the embedded blocks were equilibrated at −20 °C for 20 min and mounted onto a cryostat (Leica, Germany).Adhesive cryofilm tape (Leica, 39475214) was applied to the target region, and hard-tissue frozen sections were prepared at a thickness of 25 μm. Following sectioning, the tape carrying the tissue section was placed onto glass slides precoated with adhesive resin (Norland, NOA63). The slides were subsequently exposed to ultraviolet light for 10-15 s to polymerize the adhesive into a solvent-resistant solid layer. Finally, the adhesive tape was carefully removed, and the intact hard-tissue frozen sections were subjected to subsequent staining and fluorescence analyses.

2.16. Cartilage explants permeation

To investigate the penetration and retention of nanoparticles in the cartilage, cartilage blocks were harvested from 7-day-old C57BL/6 mice and cultured in DMEM supplemented with 10% FBS and 1% antibiotics in 24-well plates at 37 °C and 5% CO_2. The explants were then treated with different DiR-labeled formulations (200 μg/mL) for 48 h. To more clearly assess nanoparticle penetration and retention within the cartilage explants, the tissues were transferred to 1.5 mL tubes and subjected to 3-5 washes on a shaker, each lasting 30 min, to remove loosely bound particles from the surface. The explants were subsequently embedded and cryosectioned, followed by DAPI staining, and nanoparticle penetration and retention were evaluated using confocal microscopy.

2.17. Multicellular cartilage spheroids

Multicellular cartilage spheroids were generated using the hanging drop method. Briefly, chondrocytes were suspended in DMEM supplemented with 1.5% methylcellulose at a density of 1×10^6 cells/mL. Aliquots of 20 μL cell suspension were carefully pipetted onto the inner surface of a multiwell plate lid, which was then inverted and placed over the corresponding dish. The cultures were maintained in a humidified incubator at 37 °C with 5% CO_2. After three days of incubation, spheroids were formed and subsequently collected into sterile 1.5 mL tubes for further processing.

2.18. Single-cell RNA sequencing analysis

After quality control and doublet removal, 19,823 high-quality single cells from *Fgfr3*$^{+/+}$ and *Fgfr3*$^{V376D/+}$ (n = 3 per group) were retained for downstream analysis, including 9083 cells from the *Fgfr3*$^{V376D/+}$ and 10,740 cells from the *Fgfr3*$^{+/+}$ group. Cells were filtered using Seurat (version 5.0.3) based on the number of detected genes and mitochondrial transcript proportion. Specifically, genes expressed in fewer than three cells were excluded, and cells with nFeature_RNA ≤500 or percent. mt ≥ 20% were removed. Potential doublets and multiplets were further identified and excluded using DoubletFinder (version 2.0). Batch effects across samples were corrected using Harmony (version 0.1). Chondrocyte-related clusters were annotated according to canonical markers, including *Acan, Col2a1, Col9a1*, and *Col9a2*, together with cluster-specific marker genes. Differential expression analysis was performed using the FindAllMarkers function in Seurat with the Wilcoxon rank-sum test followed by Benjamini-Hochberg correction for multiple testing. The raw and processed scRNA-seq datasets generated in this study have been deposited in the NCBI Sequence Read Archive (SRA) under BioProject accession number PRJNA1463092.

2.19. Transcriptome sequencing

Total RNA was extracted from primary chondrocytes isolated from *Fgfr3*$^{V376D/+}$ mice following incubation with PBS or 1 μM PM for 24 h. RNA sequencing was performed by GENEWIZ (Suzhou, China). Briefly, poly(A)$^+$ mRNA was enriched from total RNA and used for cDNA library construction, followed by paired-end sequencing (2 × 150 bp) on an Illumina platform. Raw sequencing reads were processed using Fastp (v0.24.1) for quality control and aligned to the reference genome using HISAT2 (v2.2.1). Gene expression levels were quantified using HTSeq (v0.6.1), and differential expression analysis was performed using DESeq2 (v1.34.0). Genes with an absolute $\log_2$ fold change ≥1 and a false discovery rate (FDR) < 0.05 were considered differentially expressed. Heatmaps and volcano plots were generated using R software, and Gene Set Enrichment Analysis (GSEA) was performed to identify significantly enriched biological pathways and signaling processes.

2.20. In vivo experiments in HCH mice

Three-week-old male *Fgfr3*$^{+/+}$ and *Fgfr3*$^{V376D/+}$ mice were used in this study. The mice were divided into six groups (n = 8 per group), including a control group (*Fgfr3*$^{+/+}$ mice treated with PBS) and a PBS group (*Fgfr3*$^{V376D/+}$ mice treated with PBS), a PLGA-NPs-PM group (*Fgfr3*$^{V376D/+}$ mice treated with PLGA-NPs-PM), an RM-NPs-PM group (*Fgfr3*$^{V376D/+}$ mice treated with RM-NPs-PM), a CM-NPs-PM group (*Fgfr3*$^{V376D/+}$ mice treated with CM-NPs-PM), and a CT-CM-NPs-PM group (*Fgfr3*$^{V376D/+}$ mice treated with CT-CM-NPs-PM). For the treatment groups, the indicated nanoparticles were administered via tail vein injection at a dose of 1 mg/kg once every two days, while the control groups received an equal volume of PBS. Body weight and body length were recorded prior to each administration until the mice reached 8 weeks of age. At the end of the experiment (8 weeks of age), all mice were sacrificed, and tissues including the heart, liver, spleen, lung, kidneys, femurs, and serum samples were collected for subsequent analyses.

2.21. μ-CT and bone histomorphometry analysis

The right femurs were fixed in 4% paraformaldehyde for 24 h, followed by dehydration in 75% ethanol for subsequent micro-CT analysis. Cortical and trabecular bone morphometric parameters in the distal femur were assessed using a high-resolution micro-computed tomography system (μCT, SkyScan, USA). Image reconstruction was performed using the NRecon software, and quantitative analysis was conducted

with the CTAn program as described [34].

2.22. Bone tissue staining

Briefly, bone tissues were fixed in ice-cold 4% paraformaldehyde overnight, decalcified in 0.5 M EDTA at 4 °C with constant shaking, and subsequently embedded in paraffin wax. After deparaffinization and hydration, sections were stained with Safranin O/Fast Green, Toluidine blue and hematoxylin-eosin (H&E) according to a previously published protocol [34]. Cartilage morphology in the growth plate region was examined using a Motic VM1 digital microscope (Motic, China).

2.23. Statistical analysis

Data are presented as means ± SD. Statistical significance between two groups was determined using a two-tailed Student's *t*-test. For comparisons among more than two groups, one-way analysis of variance (ANOVA) followed by Tukey's post hoc test was performed. All statistical analyses were conducted using GraphPad Prism 10.1. $P < 0.05$ was considered statistically significant, denoted as $^{*}P < 0.05$, $^{**}P < 0.01$, $^{***}P < 0.001$, and ns (not significant) for $P > 0.05$. Each experiment was independently repeated at least three times, and representative results are presented.

3. Results

3.1. Preparation and characterization of CT-CM-NPs

To construct a chondrocyte membrane-based nanocarrier with both circulation stability and efficient penetration into growth plate cartilage, we employed a surface modification strategy. The cartilage-targeting peptide WYRGRL, which exhibits high affinity for type II collagen (COL II), was selected as the targeting ligand for nanoparticle modification [35,36]. DSPE-PEG_{2k}-WYRGRL was synthesized by conjugating WYRGRL to DSPE-PEG_{2k}-NHS via NHS ester–amine coupling, and successful conjugation confirmed by HRESIMS (Fig. S1). To maintain the surface characteristics of primary chondrocytes, P1 chondrocyte membranes were isolated by ultrasonication and density gradient centrifugation to preserve native chondrocyte properties, yielding CM vesicles (Fig. S2). The obtained vesicles were subsequently mixed with DSPE--PEG_{2k}-WYRGRL at a ratio of 2:1 to generate CT-CM vesicles (Fig. S3A). To achieve efficient drug loading, PLGA nanoparticles (PLGA-NPs) were prepared as the core of the delivery system and subsequently coated with CT-CM vesicles via co-extrusion to obtain CT-CM-NPs (Fig. 2A). Optimization of the PLGA-to-membrane ratio revealed that a 3:1 mass ratio provided the most stable formulation, with a membrane coating efficiency of 90% (Fig. S3B).

We then characterized the physicochemical properties of the prepared nanoparticles. The diameters of PLGA-NPs, CM vesicles, CM-NPs, and CT-CM-NPs were 128.40 ± 11.06 nm, 189.60 ± 6.76 nm, 141.86 ± 15.39 nm, and 136.90 ± 12.94 nm (Fig. S4A), respectively, consistent with transmission electron microscopy (TEM) observations (Fig. 2B). The corresponding zeta potentials were −19.89 ± 1.03 mV, −14.92 ± 1.81 mV, −14.44 ± 1.88 mV, and −15.32 ± 2.44 mV (Fig. 2C). CT-CM-NPs also showed good stability in both PBS and 10% FBS over 8 days of continuous observation (Fig. 2D and Fig. S4B). SDS-PAGE with Coomassie Brilliant Blue staining, together with Western blotting, confirmed that key membrane proteins, particularly those associated with cell-matrix and cell-cell interactions such as CD44, integrin β1, integrin α1, integrin α3, integrin α5, E-cadherin, and N-cadherin were well preserved during the coating process (Fig. 2E and F). To verify that the synthesized DSPE-PEG_{2k}-WYRGRL retained its COL II-targeting capability and to further extend its potential applicability beyond previous studies, surface plasmon resonance (SPR) analysis was performed using recombinant human Collagen alpha-1(II) chain (hCOL2A1), given the high conservation between human and murine COL II proteins. Consistent with previous reports, DSPE-PEG_{2k}-WYRGRL exhibited a dissociation constant (K_D) of approximately 1.2 μM toward hCOL2A1 (Fig. 2G), indicating that the peptide modification remained functional and preserved binding activity toward hCOL2A1. To further confirm the successful incorporation of DSPE-PEG_{2k}-WYRGRL into the vesicle membrane, Fourier transform infrared spectroscopy (FTIR) and fluorescence colocalization analyses were performed. FTIR spectra of dried DSPE-PEG_{2k}-WYRGRL, CM vesicles, and CT-CM vesicles revealed that the modified vesicles exhibited a markedly enhanced peak around ~1100 cm^{-1}, corresponding to the C-O-C stretching vibration of PEG, together with increased signals at several additional characteristic wavenumbers (Fig. 2H), supporting successful peptide incorporation. For fluorescence validation, DSPE-PEG_{2k}-WYRGRL-Cy5.5 was synthesized by conjugating a Cy5.5 fluorophore to the WYRGRL peptide. The successful conjugation was confirmed by ^{1}H NMR, and its excitation and emission maxima were determined to be 678 nm and 704 nm, respectively, using a fluorescence spectrophotometer (Fig. S5), while vesicles were labeled with DiO for colocalization analysis. The strong overlap between Cy5.5 and DiO fluorescence signals further confirmed successful surface modification of the vesicles (Fig. 2I). In addition, clear fluorescence colocalization was observed between DiO-labeled CT-CM vesicles and DiR-labeled PLGA-NPs, demonstrating successful encapsulation of the PLGA core within the CT-CM vesicles (Fig. 2J). Collectively, these results confirmed the successful fabrication of CT-CM-NPs.

3.2. In vitro cellular uptake of CT-CM-NPs by chondrocytes

To further evaluate the cellular uptake of CT-CM-NPs in vitro, we conducted uptake studies in chondrocytes. Five types of nanoparticles were constructed, namely PLGA-NPs, RM-NPs, CM-NPs, Trypsin-CM-NPs, and CT-CM-NPs using red blood cell or chondrocyte membranes. All nanoparticles were labeled with DiR and incubated with chondrocytes for 1 or 4 h, after which cellular uptake was assessed by flow cytometry and confocal microscopy (Fig. 3A). CM-NPs exhibited higher uptake than RM-NPs. However, after more than 80% of membrane proteins were digested by trypsin treatment (Fig. S6A), the uptake efficiencies of the two groups became nearly comparable, indicating that chondrocyte membrane coating enhanced nanoparticle internalization by chondrocytes, and that this effect was primarily mediated by membrane-associated proteins. Notably, CT-CM-NPs showed even greater uptake than CM-NPs, suggesting that WYRGRL peptide modification further promoted cellular uptake. To further investigate the underlying mechanism, *Col2a1* expression in chondrocytes was knocked down using siCol2a1 (Fig. S6B). We found that removal of the extracellular matrix combined with *Col2a1* knockdown significantly reduced the uptake of CT-CM-NPs by chondrocytes. These findings suggest that WYRGRL modification primarily enhances nanoparticle enrichment around chondrocytes through interactions with COL II, thereby facilitating subsequent cellular internalization (Fig. 3B and C). Collectively, these results indicate that both peptide functionalization and membrane coating contribute to the enhanced uptake of nanoparticles by chondrocytes. Confocal imaging after 4 h of incubation further corroborated these findings (Fig. 3D and E).

To further investigate whether WYRGRL modification altered the uptake pathway of CT-CM-NPs by chondrocytes, chondrocytes were pretreated with pathway inhibitors including nystatin (caveolae-mediated endocytosis inhibitor), cytochalasin D (phagocytosis inhibitor), dynasore (clathrin-dependent endocytosis inhibitor), or rottlerin (macropinocytosis inhibitor). Subsequently, DiR-labeled CM-NPs or CT-CM-NPs were incubated with the cells for 2 h, followed by flow cytometric analysis. The results demonstrated that both CM-NPs and CT-CM-NPs were primarily internalized through clathrin-mediated endocytosis and macropinocytosis, consistent with previous reports [27]. Notably, after WYRGRL modification, CT-CM-NPs exhibited an increased dependence on the clathrin-mediated endocytosis pathway, suggesting that surface peptide modification may influence the relative

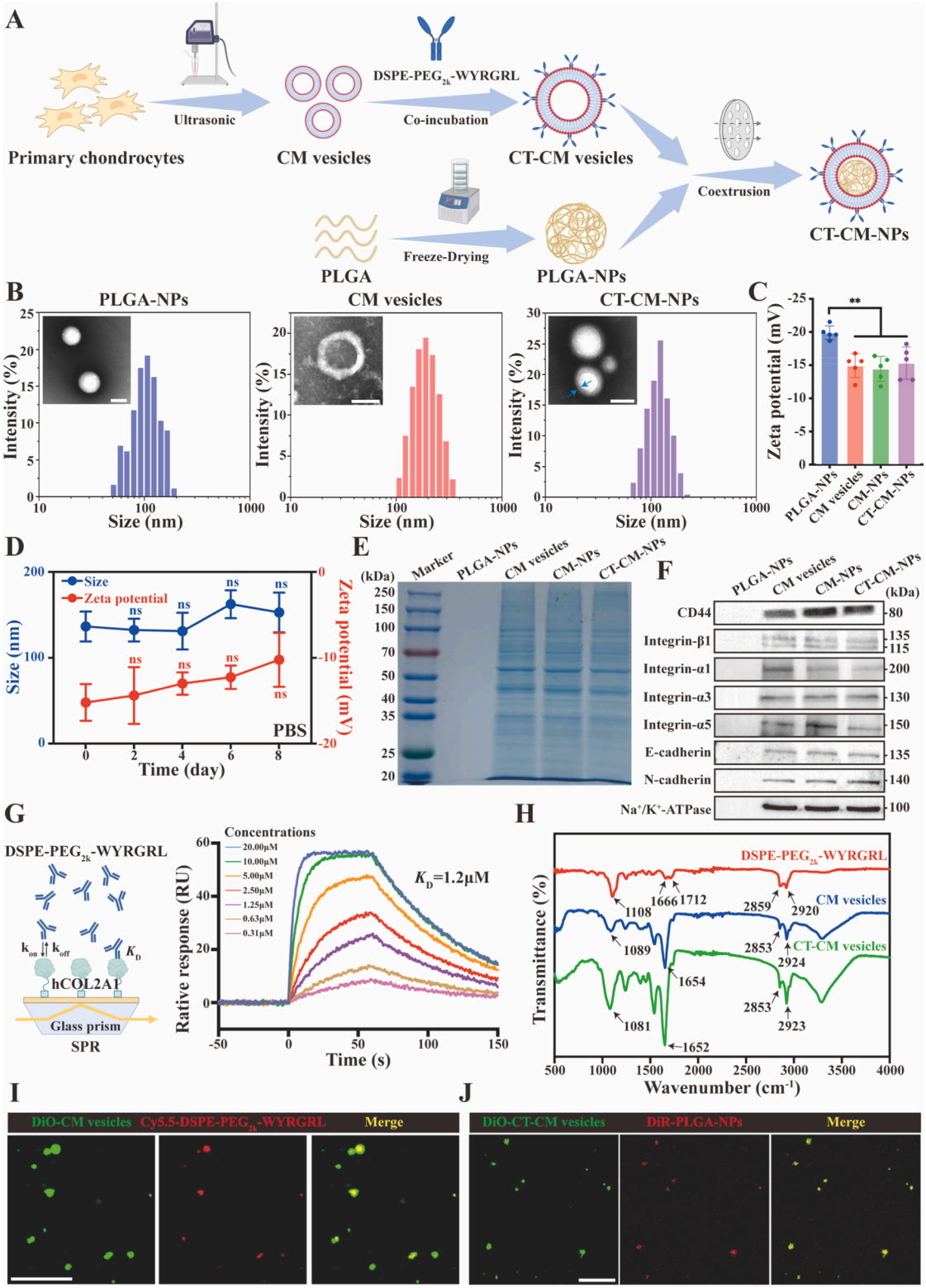

Fig. 2. Preparation and characterization of CT-CM-NPs. (A) Preparation process of CT-CM-NPs. (B) Hydrodynamic size distributions and representative TEM images of PLGA-NPs, CM vesicles and CT-CM-NPs. Scale bar, 100 nm. (C) Zeta potentials of different nanoparticles (n = 5). (D) Stability of CT-CM-NPs. Changes in particle size and zeta potential in PBS over 8 days (n = 3). (E) SDS-PAGE analysis of protein profiles in PLGA-NPs, CM vesicles, CM-NPs and CT-CM-NPs. (F) Representative western blots analysis of membrane-associated proteins in PLGA-NPs, CM vesicles, CM-NPs, and CT-CM-NPs. Marker indicates molecular weight (kDa). (G) SPR analysis of the interaction between DSPE-PEG$_{2k}$-WYRGRL and hCOL2A1. (H) FTIR analysis of DSPE-PEG$_{2k}$-WYRGRL, CM vesicles, and CT-CM vesicles. (I) Representative confocal images of colocalization between CM vesicles (green, DiO) and DSPE-PEG$_{2k}$-WYRGRL (red, Cy5.5). Scale bar, 2 μm. (J) Representative confocal images of colocalization between CT-CM vesicles (green, DiO) and PLGA-NPs (red, DiR). Scale bar, 2 μm. Statistical analysis was performed using one-way ANOVA followed by Tukey's post-hoc test. Data are presented as mean ± SD, ns: not significant, $^{*}P < 0.05$, $^{**}P < 0.01$, and $^{***}P < 0.001$.

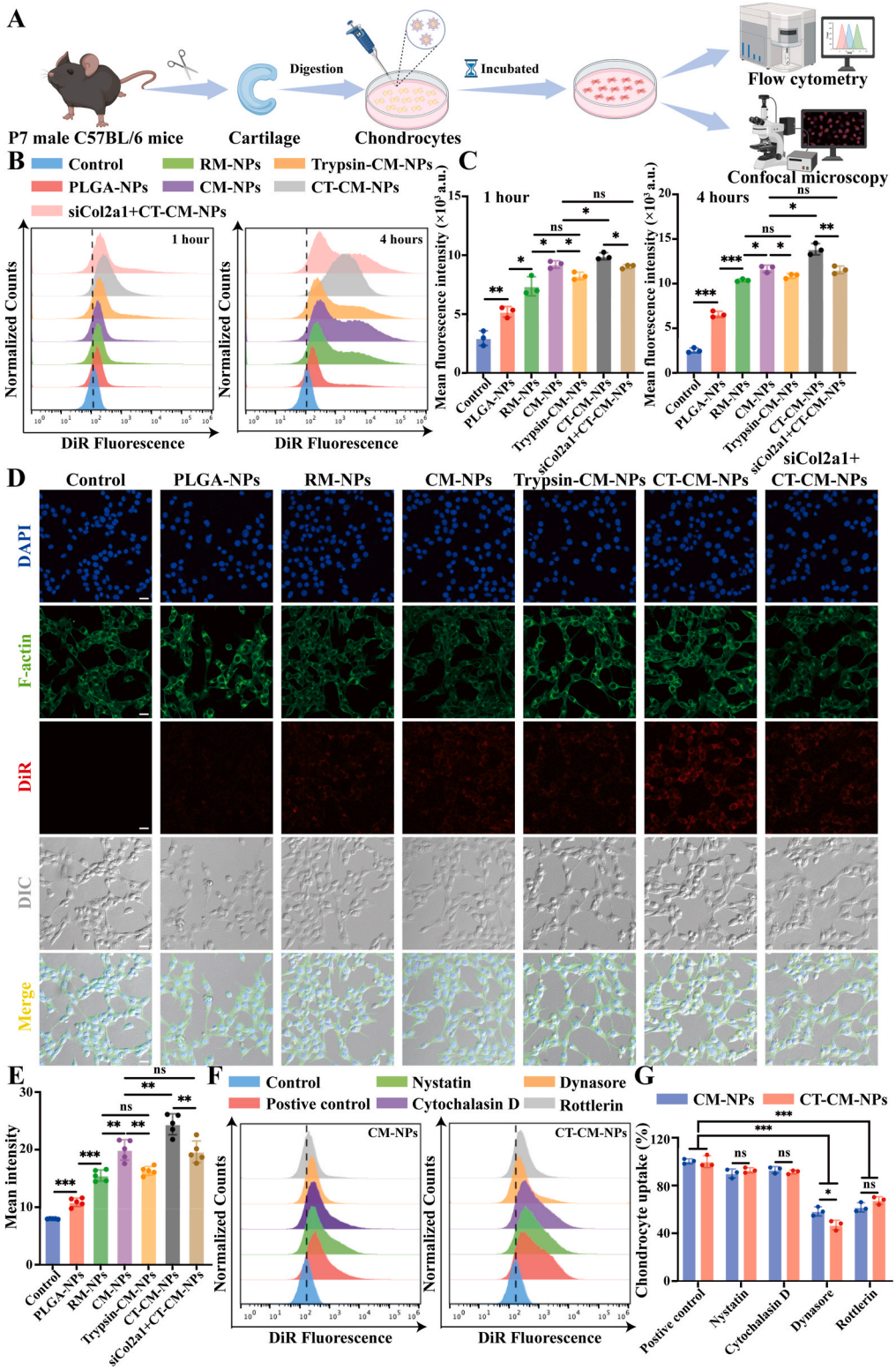

Fig. 3. In vitro uptake of CT-CM-NPs by chondrocytes. (A) Schematic representation of the in vitro cellular uptake experiment. (B) Flow cytometry analysis of DiR-labeled PLGA-NPs, RM-NPs, CM-NPs, Trypsin-CM-NPs and CT-CM-NPs binding to chondrocytes, as well as CT-CM-NPs incubated with siCol2a1-pre-treated chondrocytes, after a 1-h or 4-h incubation. (C) Quantification of the mean fluorescence intensity (n = 3). (D) Representative confocal images of chondrocytes after 4-h incubation with DiR-labeled nanoparticles. Scale bar, 20 μm. (E) Quantitative analysis of mean fluorescence intensity from confocal images (n = 5). (F) Endocytosis pathway analysis of DiR-labeled CM-NPs and CT-CM-NPs in chondrocytes. Cells were pre-treated with nystatin (caveolae-mediated), cytochalasin D (phagocytosis), dynasore (clathrin-dependent), or rottlerin (macropinocytosis). (G) Relative fluorescence intensity of DiR-positive cells following inhibitor treatment (n = 3). Statistical analysis was performed using one-way ANOVA followed by Tukey's post-hoc test. Data are presented as mean ± SD, ns: not significant, $^{*}P < 0.05$, $^{**}P < 0.01$, and $^{***}P < 0.001$.

contribution of specific uptake mechanisms (Fig. 3F and G). In contrast, similar experiments in RAW264.7 cells revealed no significant differences among the membrane-coated nanoparticle groups, confirming the chondrocyte-specific nature of this enhancement (Fig. S7).

3.3. Targeted delivery of CT-CM-NPs in vivo

Subsequently, we evaluated the in vivo targeting performance of the nanoparticles. DiR-labeled PLGA-NPs, RM-NPs, CM-NPs, and CT-CM-NPs were administered via tail vein injection, followed by fluorescence imaging of the right hindlimb at 8, 16, 24, 48, and 72 h post-injection. In parallel, distal femurs from both hind limbs were harvested at the corresponding time points to assess fluorescence accumulation within the growth plate regions (Fig. 4A and Fig. S8A). CT-CM-NPs exhibited markedly superior targeting efficiency throughout the entire administration period, suggesting that WYRGRL peptide modification significantly enhances cartilage targeting. All groups gradually reached peak accumulation in the target region at approximately 24 h post-injection, followed by a progressive decline in fluorescence intensity. Prior to 48 h, CM-NPs and RM-NPs exhibited comparable delivery efficiency in the hindlimb region. However, after 48 h, CM-NPs showed relatively stronger fluorescence retention, which may be attributable to enhanced particle retention mediated by the chondrocyte membrane coating. Notably, although RM-NPs exhibited higher fluorescence accumulation in the right hindlimb compared with PLGA-NPs, no obvious difference in cartilage-region enrichment was observed between these two groups, indicating that red blood cell membrane coating alone provided limited benefit for nanoparticle penetration or retention within cartilage tissue. In contrast, CM-NPs displayed more evident cartilage enrichment during the middle-to-late stages of circulation, particularly after 24 h (Fig. 4B–E). Ex vivo organ imaging further demonstrated that all nanoparticle formulations exhibited similar overall metabolic trends, with fluorescence signals peaking at approximately 24 h followed by gradual clearance. Moreover, aside from the unavoidable liver accumulation caused by nonspecific lipid uptake, the modified nanoparticles exhibited markedly reduced accumulation in the lung and spleen, while showing enhanced fluorescence distribution in femoral regions, particularly around the distal femur, at multiple time points (Fig. S8B and C). To further verify nanoparticle enrichment within the growth plate, femurs were collected from mice 24 h after treatment with different nanoparticle formulations, followed by hard-tissue sectioning and fluorescence analysis of the growth plate region. The results demonstrated prominent DiR fluorescence accumulation within the growth plate in the CT-CM-NPs group (Fig. 4F and G). Collectively, WYRGRL peptide modification primarily enhanced nanoparticle targeting and enrichment around cartilage tissue, whereas chondrocyte membrane coating mainly contributed to prolonged particle retention within the target region.

3.4. Penetration and retention of nanoparticles in cartilage

Due to the structural characteristics of the growth plate cartilage, conventional nutrients must enter and be taken up by chondrocytes through diffusion. Therefore, an effective nanoparticle delivery system should not only accumulate in the surrounding regions but also penetrate deeply into cartilage tissue. Previous studies have reported that coating nanoparticles with chondrocyte membranes enables this process by facilitating direct cell-matrix and cell-cell interactions. To assess the cartilage penetration of CT-CM-NPs, we employed multicellular spheroids (MTS), a three-dimensional (3D) in vitro model that mimics native cartilage tissue. Five types of DiR-labeled nanoparticles were incubated with mouse chondrocyte MTS for 6 or 12 h, followed by confocal microscopy Z-stack imaging at 25-μm intervals (Fig. 5A). As a result, fluorescence signals from PLGA-NPs, RM-NPs, and Trypsin-CM-NPs were weak and mostly restricted to the spheroid surface, whereas CM-NPs and CT-CM-NPs exhibited strong and comparable signals penetrating into deeper layers. Moreover, chondrocyte membrane coating enabled the nanoparticles to progressively penetrate deeper into the MTS over time, reaching the spheroid core. These findings indicate that chondrocyte membrane coating markedly enhances nanoparticle penetration within MTS (Fig. 5B and C).

To further validate these findings, we conducted studies using mouse cartilage explants, which better replicate the dense native cartilage structure and present a greater challenge to penetration. Immunofluorescence analysis was used to evaluate nanoparticle retention and penetration (Fig. 5D). After 48 h of incubation, explants treated with CM-NPs or CT-CM-NPs displayed markedly greater nanoparticle retention and deeper penetration than those treated with PLGA-NPs, RM-NPs, or Trypsin-CM-NPs, indicating that chondrocyte membrane coating effectively enhances particle localization within cartilage. Notably, after multiple washes of the explants to remove loosely bound nanoparticles, fluorescence signals from PLGA-NPs, RM-NPs, or Trypsin-CM-NPs, were nearly undetectable (Fig. 5E and F). Collectively, this result demonstrates that chondrocyte membrane modification substantially enhances nanoparticle retention and penetration in cartilage, providing an effective strategy for targeted drug delivery to growth plate cartilage. However, we were also surprised to find that surface peptide modification conferred minimal additional benefit in penetration and retention.

3.5. Ciliogenesis defects and hedgehog pathway suppression in *Fgfr3*$^{V376D/+}$ mice

Consistent with our previous report, *Fgfr3*$^{V376D/+}$ mice modeling HCH were generated using CRISPR/Cas9 [31] (Fig. 6A and Fig. S9). At 4 weeks of age (prepubertal stage), these mice displayed pronounced developmental defects compared with *Fgfr3*$^{+/+}$ (wild-type littermates), including reduced body length, shortened femurs, and markedly decreased bone mass (Fig. 6B–H and Fig. S10). Histological analysis of the growth plate cartilage revealed significant narrowing in *Fgfr3*$^{V376D/+}$ mice, as shown by Safranin O/Fast Green and H&E staining (Fig. 6I and J). Further H&E analysis indicated that this reduction was primarily attributable to a decrease in the columnar zone (CZ) and hypertrophic zone (HZ), accompanied by a partial expansion of the resting zone (RZ), reflecting a pronounced shift toward quiescence in the growth plate cartilage of HCH mice (Fig. 6K).

To further investigate the underlying mechanisms, cells were isolated from the distal femur and proximal tibia of *Fgfr3*$^{+/+}$ and *Fgfr3*$^{V376D/+}$ mice, followed by digestion, cell sorting, and single-cell RNA sequencing (Fig. S11). Chondrocyte clusters were extracted for downstream analysis, revealing significant transcriptional differences between the two mouse models (Fig. 6L). Notably, genes related to Hedgehog signaling and ciliogenesis were markedly downregulated in *Fgfr3*$^{V376D/+}$ chondrocytes (Fig. 6M and N). To validate these findings, chondrocytes from 7-day-old mice were isolated, expanded in vitro, and subjected to protein analysis (Fig. 6O). Western blotting demonstrated decreased expression of IHH (Hedgehog pathway protein) and Ace α-tubulin (cilia-associated protein) in *Fgfr3*$^{V376D/+}$ chondrocytes, consistent with the single-cell RNA-seq results (Fig. 6P and Q). Histological sections and immunofluorescence staining further corroborated the downregulation of Hedgehog signaling and impaired ciliogenesis in the HCH mice (Fig. 6R–T). These phenotypes are consistent with prior observations in ACH, though with relatively attenuated severity. Modulation of the Hedgehog signaling pathway has been reported to restore primary ciliary function and alleviate skeletal abnormalities associated with ACH [15]. Based on these findings, the Hedgehog pathway agonist Purmorphamine (PM) was selected as a potential therapeutic agent for the treatment of HCH [37,38]. To investigate the effects of PM on chondrocytes, primary chondrocytes were isolated from P7 *Fgfr3*$^{V376D/+}$ mice, treated with PM in vitro, and subsequently subjected to transcriptomic analysis. The results revealed that PM markedly activated Hedgehog signaling and multiple proliferation-related pathways, accompanied by upregulation of genes associated with chondrocyte

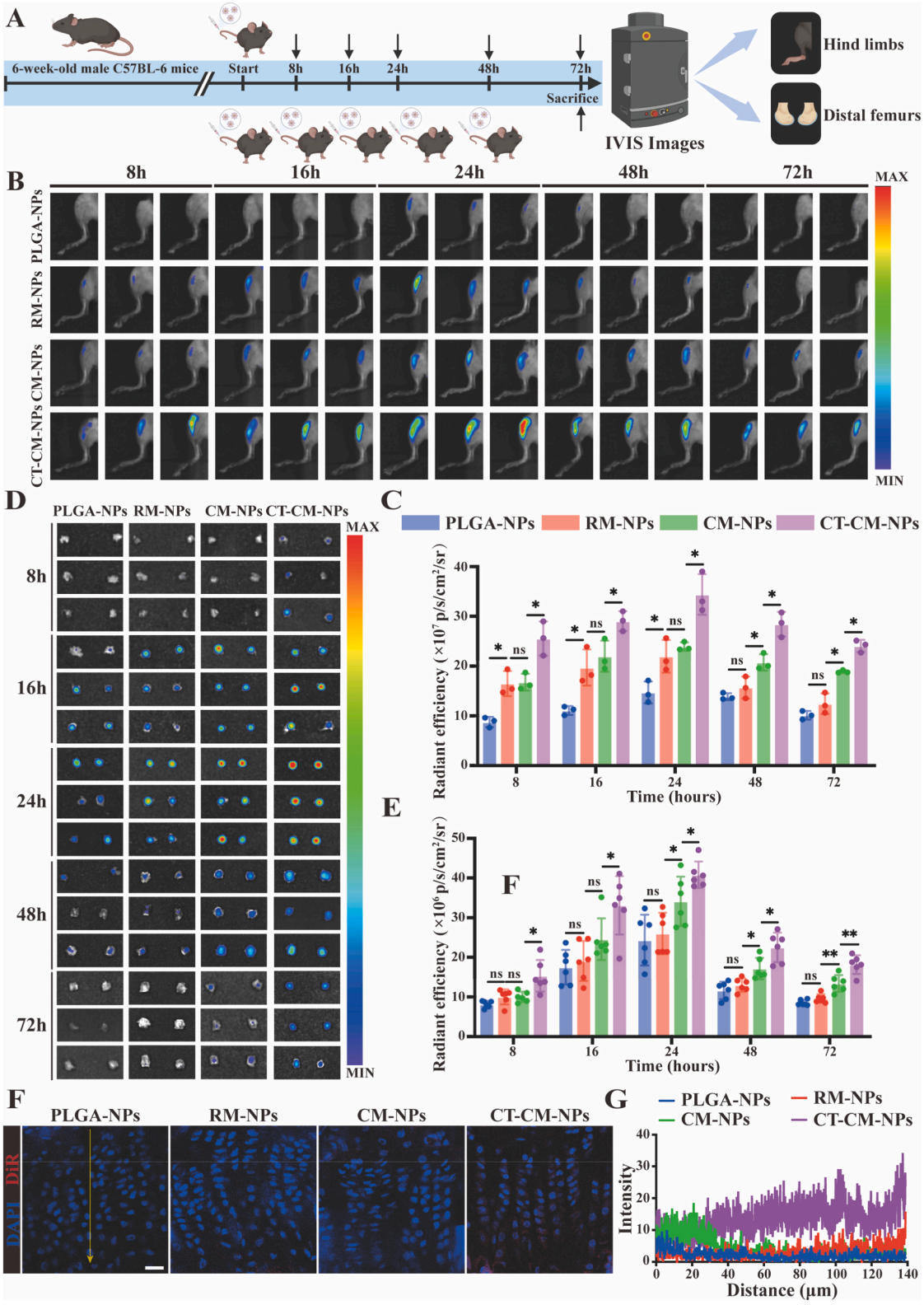

Fig. 4. Targeting ability of CT-CM-NPs to growth plate cartilage regions in vivo. (A) Schematic illustration of the in vivo targeting experiment. (B) Representative IVIS images showing the biodistribution and retention of DiR-labeled PLGA-NPs, RM-NPs, CM-NPs, and CT-CM-NPs in the hind limbs at 8, 16, 24, 48, and 72 h post-injection. (C) Quantitative analysis of normalized time-course fluorescent radiant efficiency in the hind limbs (n = 3). (D) Representative ex vivo IVIS images showing the accumulation of DiR-labeled nanoparticles in the distal femoral cartilage regions of both hind limbs at 8, 16, 24, 48, and 72 h following a single intravenous injection. (E) Quantitative analysis of normalized fluorescence radiant efficiency in the distal femoral regions over time (n = 6 from 3 mice). (F) Representative confocal immunofluorescence images of hard-tissue cryosections from growth plate regions following different nanoparticle treatments. Nanoparticles (red, DiR), nuclei (blue, DAPI). Scale bars, 20 μm. (G) Fluorescence intensity profiles of different nanoparticles across the growth plate region. Statistical analysis was performed using one-way ANOVA followed by Tukey's post-hoc test. Data are presented as mean ± SD, ns: not significant, $^{*}P < 0.05$, and $^{**}P < 0.01$.

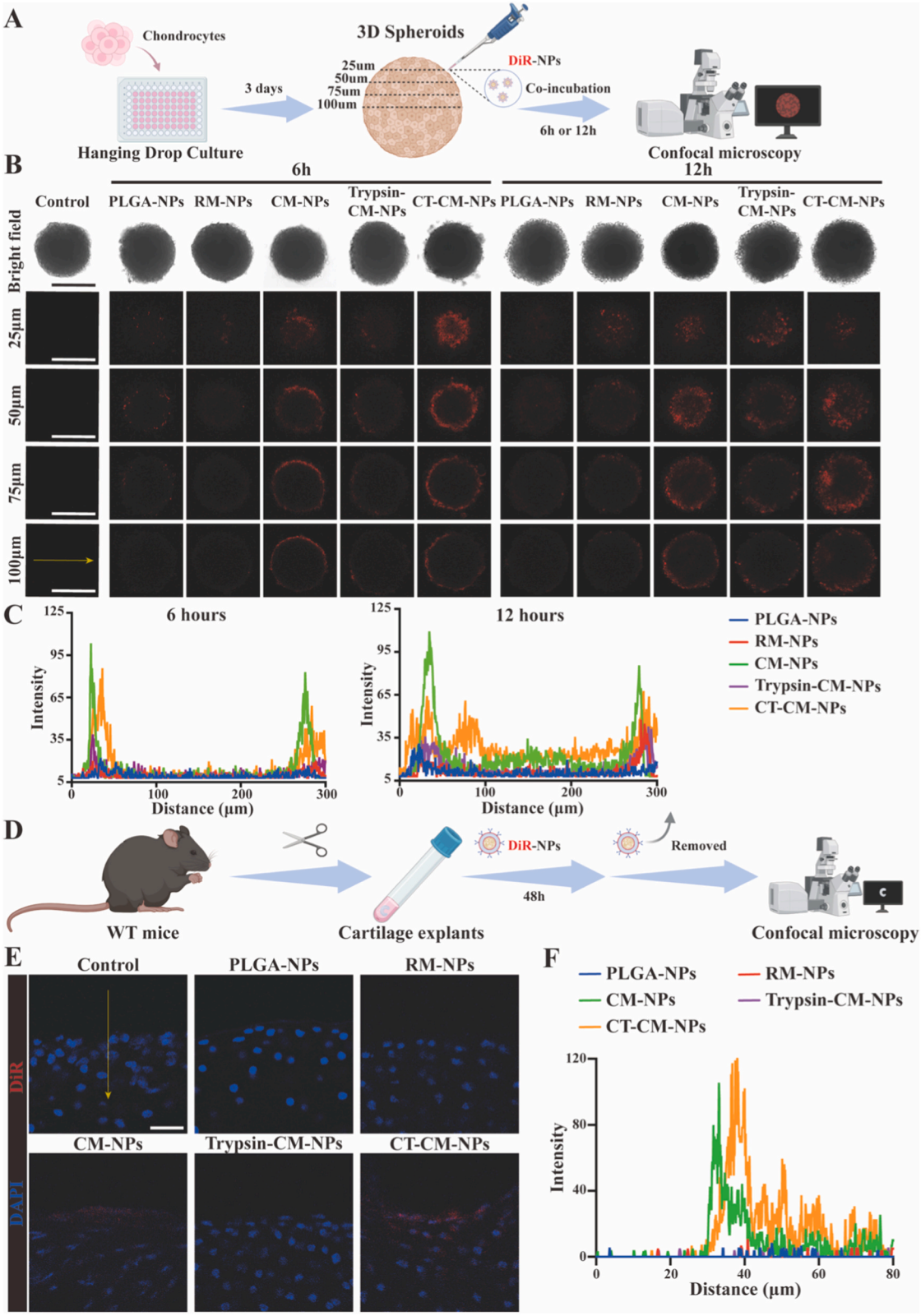

Fig. 5. Chondrocyte membrane coating significantly enhances the penetration and retention of nanoparticles. (A) Schematic illustration of confocal imaging to assess the effect of DiR-labeled nanoparticles on the penetration of MTS. (B) Representative confocal images of MTS following 6 and 12 h of nanoparticle incubation, captured at 25-μm intervals from top to bottom (n = 5). Nanoparticles (red, DiR). Scale bar, 200 μm. (C) Representative fluorescence intensity profile of indicated nanoparticles across an MTS section (100 μm height). (D) Schematic of the experimental setup used to evaluate the penetration and retention in cartilage explants. (E) Representative confocal images of cartilage explant cross-sections after 48 h of incubation with indicated nanoparticles. Nanoparticles (red, DiR), nuclei (blue, DAPI). Scale bars, 20 μm. (F) Fluorescence intensity profile of different nanoparticles across the cartilage explant section.

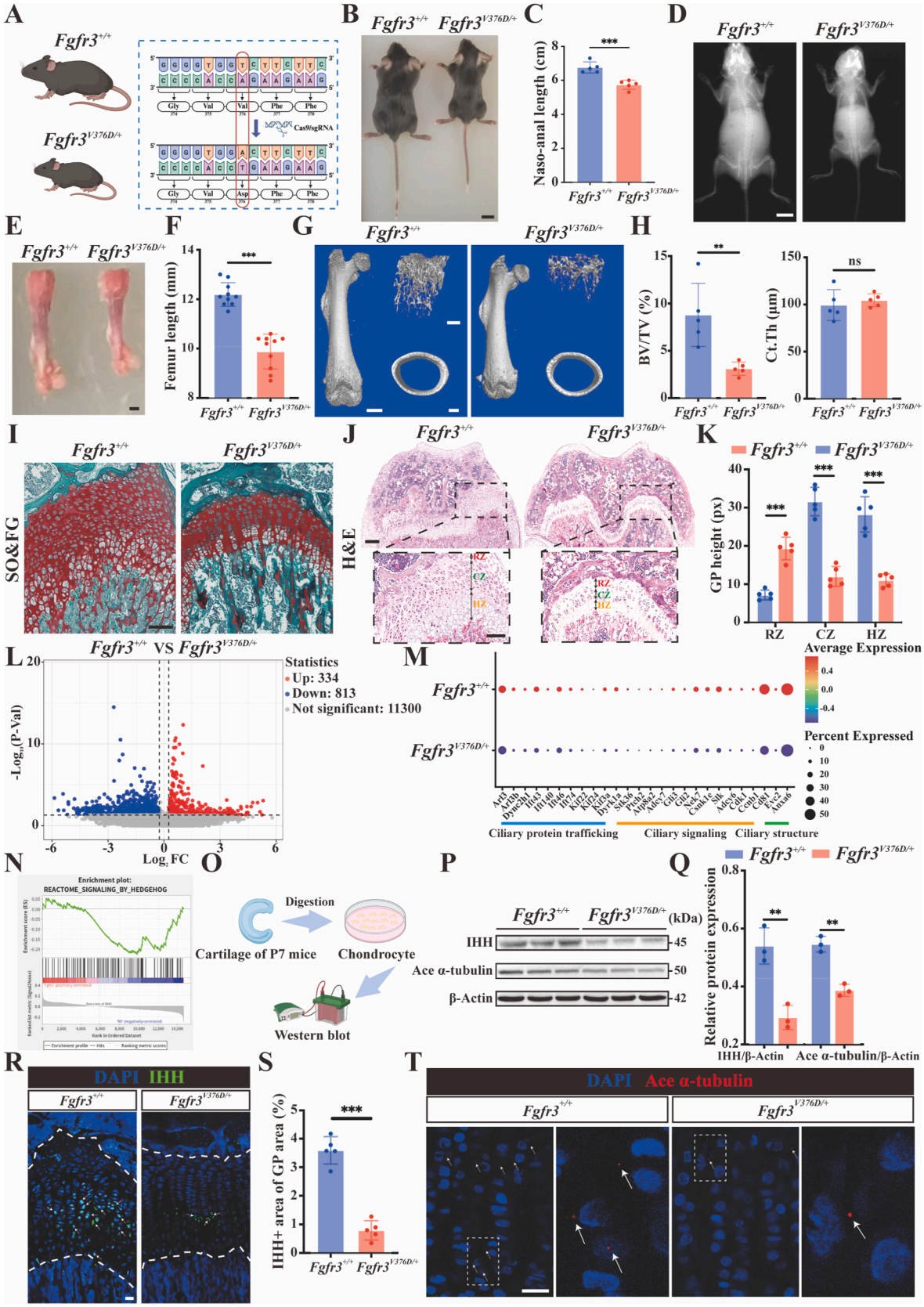

(caption on next page)

Fig. 6. Ciliary defects and Hedgehog pathway suppression in *Fgfr3*$^{V376D/+}$ mice. (A) Schematic diagram of the generation of *Fgfr3*$^{V376D/+}$ mice using CRISPR/Cas9. (B) Representative images showing differences in naso-anal lengths between 4-week-old *Fgfr3*$^{+/+}$ and *Fgfr3*$^{V376D/+}$ mice. Scale bars, 1 cm. (C) Quantification and statistical analysis of naso-anal length (n = 5). (D) Representative X-ray images of *Fgfr3*$^{+/+}$ and *Fgfr3*$^{V376D/+}$ mice. Scale bars, 1 cm. (E and F) Representative images and quantification of femur length in the same mice shown in C (n = 10 from 5 mice). Scale bars, 1 mm. (G) Representative μCT reconstruction images. Scale bars, 1 mm (left) or 250 nm (right). (H) Quantification of bone volume/tissue volume (BV/TV) and cortical thickness (Ct.Th) (n = 5). (I) Representative images of Safranin O/Fast Green–stained growth plates. Scale bars, 100 μm. (J) H&E-stained sections of distal femoral growth plates. Scale bars, 100 μm. (K) Quantification of growth plate zone heights (n = 5). (L) Volcano plot of differentially expressed genes (DEGs) in chondrocytes from *Fgfr3*$^{V376D/+}$ and *Fgfr3*$^{+/+}$ mice ($Log_2FC \geq 1$ and $P \leq 0.05$). (M) Dot plot showing differential expression of cilia-related genes in *Fgfr3*$^{V376D/+}$ and *Fgfr3*$^{+/+}$. (N) GSEA enrichment analysis of Hedgehog signaling in chondrocytes from *Fgfr3*$^{V376D/+}$ and *Fgfr3*$^{+/+}$ mice. (O) Schematic illustration of the chondrocyte isolation procedure. (P) Representative Western blot analysis of IHH and Ace α-tubulin expression. (Q) Quantitative analysis of the relative protein expression of IHH and Ace α-tubulin (n = 3). (R) Immunofluorescence staining of IHH (green) and nuclei (DAPI, blue) in growth plates. Scale bars, 20 μm. (S) Quantitative analysis of IHH$^+$ area within growth plates relative to control (n = 5). (T) Immunofluorescence staining of Ace α-tubulin (red) and nuclei (blue, DAPI) in growth plates. Scale bars, 20 μm. Statistical analysis was performed using unpaired two-tailed student's t-test. Data are presented as mean ± SD, ns: not significant, $^{**}P < 0.01$, and $^{***}P < 0.001$.

maturation and function. Consistently, protein-level validation demonstrated increased expression of the representative Hedgehog pathway marker GLI1 following PM treatment, further supporting activation of Hedgehog signaling in chondrocytes and suggesting that PM promotes chondrocyte proliferation and maturation primarily through Hedgehog pathway activation (Fig. S12).

Encouraged by the regulatory effects of PM on Hedgehog signaling and chondrocyte function, we further incorporated PM into our chondrocyte membrane-coated nanocarrier system to generate CT-CM-NPs-PM, aiming to improve its systemic delivery efficiency and therapeutic efficacy. The resulting biomimetic nanoparticles were subsequently investigated in both in vitro and in vivo models to assess their therapeutic potential for the systemic treatment of HCH.

3.6. CT-CM-NPs-PM promotes hedgehog pathway activation, ciliogenesis, and chondrocyte proliferation in vitro

To achieve efficient delivery of PM to the growth plate cartilage of HCH mice, we constructed CT-CM-NPs-PM drug-loaded nanoparticles. Using a microemulsion method, the hydrophobic drug PM was successfully encapsulated into PLGA. Optimization studies revealed that a PLGA:PM mass ratio of 10 yielded the highest encapsulation performance, achieving an encapsulation efficiency of approximately 72.59% and a drug loading capacity of 7.73% (Fig. 7A and Figs. S13 and S14). The release profile of PM was sustained and stable, with about 68.18% of the drug released within two days. Notably, although sustained drug release was not a primary objective in the design of this delivery system, both membrane coating and PEG modification moderately delayed PM release during in vitro release analysis (Fig. 7B). To evaluate biosafety, PLGA-NPs-PM, RM-NPs-PM, CM-NPs-PM, and CT-CM-NPs-PM were tested in primary chondrocytes, ATDC-5 cells (a chondrocyte cell line), and RAW264.7 cells. The results demonstrated that these nanoparticles exhibited acceptable biocompatibility at the cellular level (Fig. 7C and Fig. S15).

Subsequently, we conducted in vitro validation experiments (Fig. 7D). CT-CM-NPs-PM were co-incubated with chondrocytes to assess Hedgehog pathway activation. To better distinguish the drug induction efficiency under different loading modes, a short incubation protocol was applied, with drug removal after 4 h followed by an additional 2 days of culture prior to q-PCR analysis. Under these conditions, key Hedgehog target genes, including *Ptch1*, *Gli1*, and *Hhip*, were significantly upregulated. Chondrocyte membrane coating conferred higher activation efficiency, and targeted modification further enhanced this effect (Fig. 7E). We next isolated chondrocytes from different mouse sources for in vitro nanoparticle incubation and assessment of ciliogenesis, and found that PM alone modestly promoted cilia formation, whereas the combination of chondrocyte membrane coating and targeted modification markedly enhanced this effect, in line with Hedgehog pathway activation (Fig. 7F and G). To further mimic in vivo chondrocyte proliferation, MTS of uniform size were generated using the hanging-drop method, incubated with nanoparticles for 12 h, and subsequently cultured for 3 days. Analysis of spheroid diameters revealed that nanoparticles without membrane coating, or coated only with red blood cell membranes, had minimal effects on proliferation under 3D conditions. In contrast, chondrocyte membrane coating substantially promoted spheroid growth, while targeted modification provided only limited additional benefit, likely because penetration was primarily dependent on the chondrocyte membrane (Fig. 7H and I). Collectively, these results demonstrate that CT-CM-NPs-PM can effectively activate the Hedgehog pathway, promote ciliogenesis, and enhance chondrocyte proliferation in vitro.

3.7. CT-CM-NPs-PM safely restores the cartilage phenotype and alleviates developmental defects in HCH mice

For the in vivo experiments, 3-week-old *Fgfr3*$^{+/+}$ and *Fgfr3*$^{V376D/+}$ mice were selected, as the critical developmental window in mice occurs between 3 and 8 weeks of age. Based on preliminary efficacy studies, the in vitro release profile of PM, and its pharmacological activity, nanoparticles were administered via tail vein injection at a dose of 1 mg/kg every two days for five weeks. Body weight and body length were continuously monitored throughout the treatment period (Fig. 8A). The results indicated that CT-CM-NPs-PM treatment significantly increased body length in *Fgfr3*$^{V376D/+}$ mice, with the average body length reaching 8.94 cm, showing no significant difference compared with *Fgfr3*$^{+/+}$ mice. This therapeutic effect is likely attributable to the enhanced accumulation of nanoparticles within vertebral cartilage. In addition, groups receiving nanoparticles coated with red blood cell membranes also exhibited some improvement, possibly because vertebrae, which contributes substantially to overall body length, are relatively more accessible to circulating nutrients and systemically delivered agents (Fig. 8B and C, and Fig. S16A and B). Unlike the crawling locomotion of mice, the upright posture and bipedal walking of humans make long bones a critical determinant of body height. Regarding femur length, membrane coating successfully enhanced drug delivery and improved long-bone phenotypes, while chondrocyte membrane coating and additional targeted modification further strengthened these therapeutic effects (Fig. 8D and E, and Fig. S16C). Histological analysis of femurs, including Safranin O & Fast Green, Toluidine Blue, and H&E staining, revealed that CT-CM-NPs-PM promoted chondrocytes proliferation within the growth plate, particularly in columnar and hypertrophic chondrocytes (Fig. 8F–I). Immunofluorescence staining of GLI1, PTCH1, and Ace α-tubulin showed that Hedgehog signaling pathway was effectively activated under CT-CM-NPs-PM treatment, which in turn promoted ciliary regeneration in chondrocytes (Fig. 8J and K, and Fig. S17). Subsequent Ki67 immunofluorescence further supported this observation, demonstrating a significant enhancement in the proliferative capacity of chondrocytes (Fig. 8L and M).

The biosafety of this nanoparticle delivery platform was systematically evaluated. Hemolysis assays and H&E staining of major organs showed no signs of toxicity (Fig. 9A–C and Fig. S18). Subsequent ELISA experiments indicated that cell membrane coating effectively reduced the immunogenicity of the nanoparticles, while targeted modification further enhanced their biocompatibility to some extent (Fig. 9D and E).

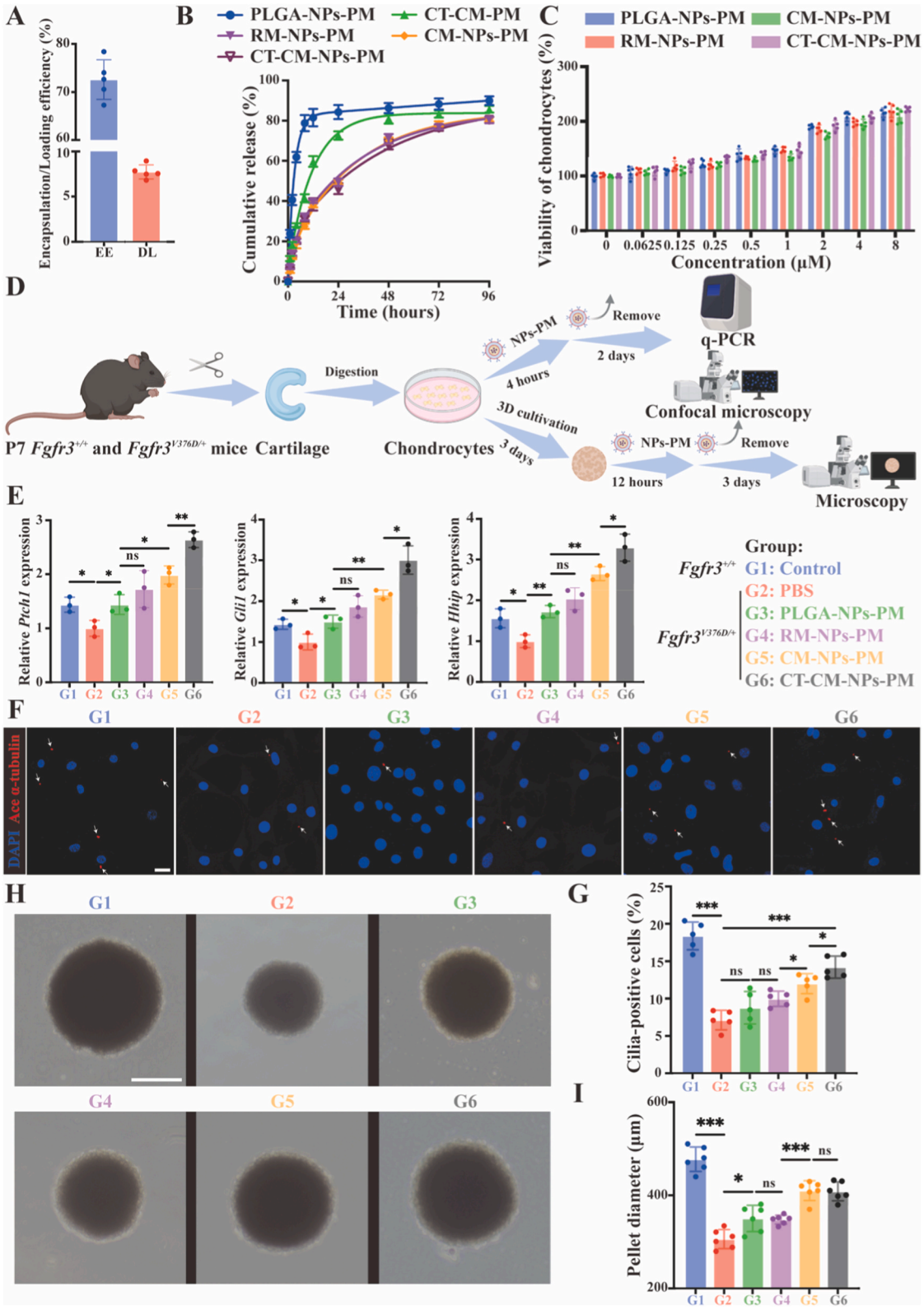

Fig. 7. CT-CM-NPs-PM promotes Hedgehog pathway activation, ciliogenesis, and chondrocyte proliferation in vitro. (A) Encapsulation and loading efficiency of PM in CT-CM-NPs (n = 5). (B) In vitro release of PM from PLGA-NPs-PM, CT-CM-PM, RM-NPs-PM, CM-NPs-PM and CT-CM-NPs-PM in PBS (pH 7.4) (n = 3). (C) Cytotoxicity of PLGA-NPs-PM, RM-NPs-PM, CM-NPs-PM, and CT-CM-NPs-PM against chondrocytes after a 24-h incubation at indicated concentrations (n = 5). (D) Schematic illustration of the in vitro validation workflow of CT-CM-NPs-PM. (E) Relative expression levels of Hedgehog target genes (*Ptch1*, *Gli1*, and *Hhip*) in chondrocytes treated with different nanoparticles (n = 3). (F) Representative immunofluorescence images of Ace α-tubulin (red) and nuclei (blue, DAPI) in chondrocytes after nanoparticle treatment. Scale bars, 20 μm. (G) Quantitative analysis of cilia-positive cells (n = 5). (H) Representative images of MTS treated with different nanoparticles. Scale bars, 200 μm. (I) Quantitative analysis of MTS diameter variation (n = 6). Statistical analysis was performed using one-way ANOVA followed by Tukey's post-hoc test. Data are presented as mean ± SD, ns: not significant, $^{*}P < 0.05$, $^{**}P < 0.01$, and $^{***}P < 0.001$.

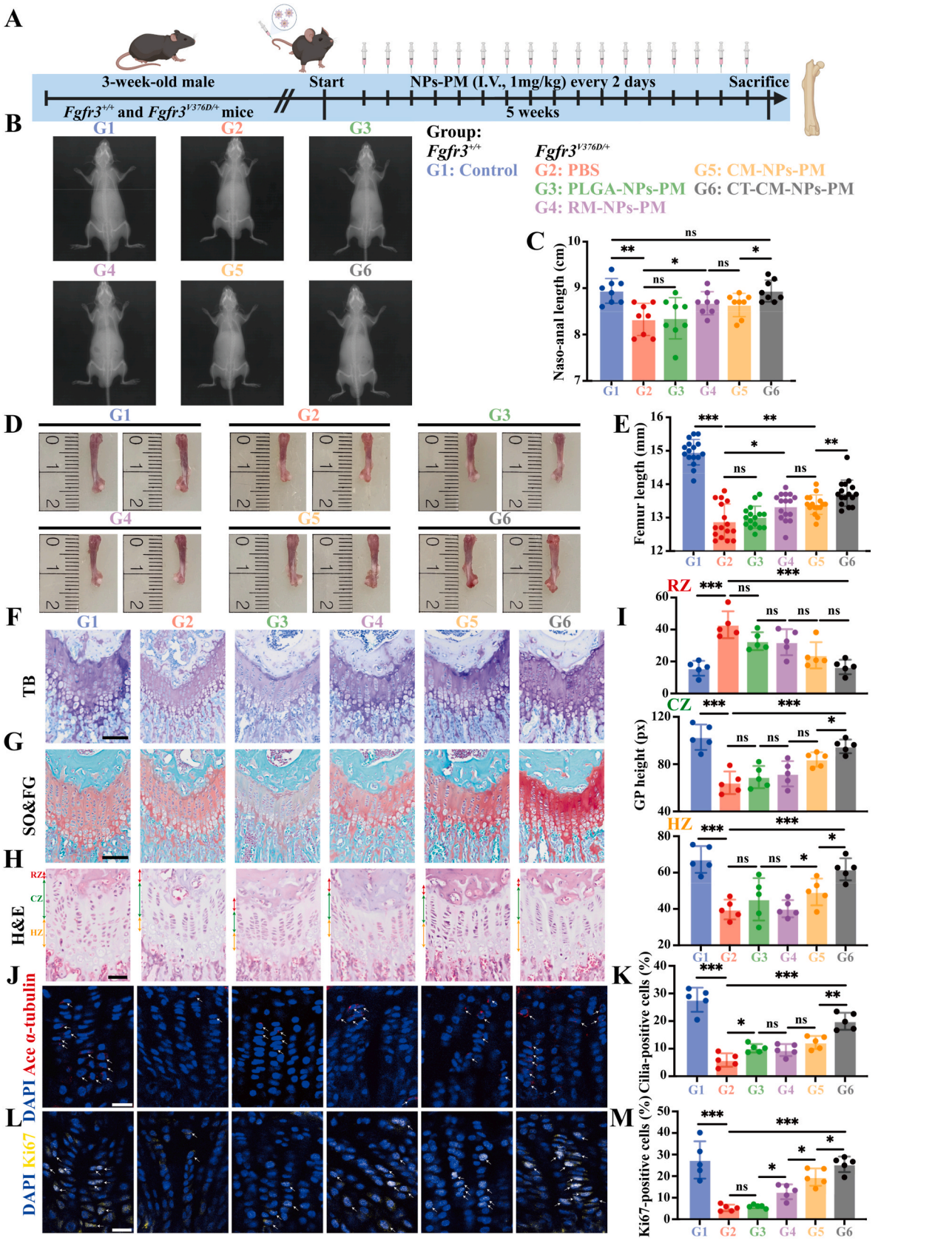

(caption on next page)

Fig. 8. CT-CM-NPs-PM restores cartilage phenotype and alleviates developmental defects in *Fgfr3*$^{V376D/+}$ mice. (A) Schematic diagram of the in vivo validation workflow for CT-CM-NPs-PM. (B) X-rays of mice subjected to different treatments. Scale bars, 1 cm. (C) Quantitative analysis of naso-anal lengths of mice (n = 8). (D) Representative femur length images of the same mice shown in C. (E) Quantitative analysis of the femur length (n = 16 from 8 mice). (F) Representative images of Toluidine blue staining of mouse GPs. Scale bars, 100 μm. (G) Representative images of SO&FG staining of GPs. Scale bars, 100 μm. (H) Pictures of H&E-stained sections of mouse GPs. Scale bars, 100 μm. (I) Quantitative analysis of GP zone heights in mice (n = 5). (J) Immunofluorescence staining of Ace α-tubulin (red) and nuclei (blue, DAPI) in GPs treated with different nanoparticles. Scale bars, 20 μm. (K) Quantitative analysis of Cilia-positive cells (n = 5). (L) Immunofluorescence staining of Ki67 (yellow) and nuclei (blue, DAPI) in GPs of mice. Scale bars, 20 μm. (M) Quantitative analysis of Ki67-positive cells within GPs, relative to control (n = 5). Statistical analysis was performed using one-way ANOVA followed by Tukey's post-hoc test. Data are presented as mean ± SD, ns: not significant, $^{*}P < 0.05$, $^{**}P < 0.01$, and $^{***}P < 0.001$.

Additional biochemical parameters were all within normal ranges, providing further evidence for the safety of this delivery system (Fig. 9F–I). Collectively, these findings demonstrate that the CT-CM-NPs-PM platform enables safe and efficient drug delivery, activates Hedgehog signaling, promotes ciliogenesis, and restores growth plate function, thereby mitigating developmental defects in HCH mice.

4. Discussion

Systemic cartilage disorders are characterized by widespread cartilage lesions, which significantly limit the applicability of current therapeutic approaches. Among them, the growth plate cartilage region represents one of the most challenging targets for systemic therapy due to its limited nutrient supply. At present, most cartilage-related studies and therapeutic strategies focus on localized repair of articular cartilage, whereas systemic treatment strategies targeting the entire cartilage system remain underdeveloped, resulting in the absence of effective and standardized therapeutic options for such diseases. In our previous work, we reported the human HCH phenotype caused by the *FGFR3*$^{G382D/+}$ mutation and established a corresponding *Fgfr3*$^{V376D/+}$ mouse model [31,39]. This mutation induces severe cartilage abnormalities, including defects in bone mass, bone length and, body length. Further studies revealed that *FGFR3* mediates disease progression by impairing chondrocyte autophagy and promoting HSPB6-mediated cuproptosis, providing potential therapeutic targets. However, in vivo validation of these strategies has been hampered by the inability to efficiently deliver drugs to growth plate cartilage, leading to unsatisfactory therapeutic outcomes.

An ideal delivery system for growth plate cartilage should, following administration, traverse the complex systemic circulation, reach target tissues, and achieve sufficient penetration to enable effective drug release deep within the cartilage. Such a nanoplatform must simultaneously ensure circulation stability, low immunogenicity, and specific targeting and penetration of cartilage. Cell membrane-based biomimetic technology provides a promising solution by coating nanoparticles with natural membranes, thereby reducing immunogenicity and enhancing circulation stability [40]. To date, this approach has primarily employed circulating cell membranes including erythrocytes, neutrophils and macrophages, with relatively little focus on resident cells [41–43]. Even in cases where resident cell membranes have been used, most studies have aimed at crossing biological barriers, without fully considering the intricate interactions between resident cells and their microenvironment shaped by long-term evolution [19]. These interactions may offer significant value and application potential for drug delivery. Given its specialized extracellular matrix and unique cellular microenvironment, cartilage presents a particularly promising target for exploration in this context [44,45]. Unlike conventional delivery systems, exemplified by liposomes [46], which are generally designed as standardized and broadly applicable platforms, cell membrane-based delivery systems are inherently more adaptable and can be tailored to specific diseases and biological contexts. Leveraging these distinctive features may open up new possibilities for cartilage-targeted therapies.

In the present study, we have fully considered the relationship between chondrocytes and their matrix and sought to address developmental abnormalities in *Fgfr3*$^{V376D/+}$ mice by constructing a growth plate-targeted delivery system based on cell membrane coating and surface modification, generating CT-CM-NPs. We systematically characterized their physicochemical properties, validated their targeting capacity both in vitro and in vivo, and assessed cartilage penetration using MTS and cartilage explant. Single-cell transcriptomic analysis of *Fgfr3*$^{V376D/+}$ mice revealed downregulation of the Hedgehog signaling pathway and abnormal ciliogenesis. To overcome these defects, we encapsulated the Hedgehog pathway agonist PM within CT-CM-NPs, obtaining CT-CM-NPs-PM. Using this system, we successfully upregulated Hedgehog pathway activity of growth plate chondrocytes, promoted ciliogenesis, and improved both cartilage phenotypes and overall development in mutant mice.

Despite these promising findings, several limitations should be noted. First, this systemic cartilage-targeted delivery platform was validated in a single disease model of HCH. Given the heterogeneous etiologies of systemic cartilage disorders, further studies are needed to confirm its applicability across different disease models. Second, our in vivo analyses primarily focused on the distal femoral growth plate, while HCH also involves multiple regions, including craniofacial and oral bone development, which require more comprehensive evaluation in future work. Third, although cartilage-targeting modifications improved delivery, some accumulation of nanoparticles in non-target organs was observed. In addition, resident cell membrane coatings may pose a higher risk of immunogenicity due to the potential incomplete removal of intracellular components, particularly genetic materials [47]. These findings highlight the need for improved targeting strategies to enhance specificity and reduce off-target distribution, such as the incorporation of peptides with higher cartilage affinity. Finally, due to the difficulty of obtaining human growth plate cartilage samples in clinical practice, we were unable to validate the functionality of the nanoparticles in human-derived samples during in vitro studies, which limits translational extension. Encouragingly, recent advances in cartilage organoid technology may provide a promising human-relevant platform for evaluating targeting efficiency and therapeutic efficacy in future studies, thereby facilitating subsequent clinical translation [48].

5. Conclusion

In conclusion, we developed a systemic cartilage-targeted delivery system in which WYRGRL modification enabled selective targeting of cartilage tissue during systemic administration, while the primary chondrocyte membrane coating endowed the nanoparticles with enhanced retention and penetration within the cartilage, including the avascular and alymphatic growth plate cartilage. By integrating the complementary functions of peptide modification and membrane camouflage, the platform achieved efficient delivery to cartilage tissue. While maintaining a favorable safety profile, the system is capable of delivering the Hedgehog pathway agonist PM to growth plate cartilage, thereby partially rescuing cartilage defects in *Fgfr3*$^{V376D/+}$ mice. Collectively, this work provides new insights for the clinical management of HCH. Further optimization and expansion of this platform may offer a reliable and versatile option for systemic drug delivery in cartilage diseases.

Ethics approval and consent to participate

All animal experiments were conducted in compliance with

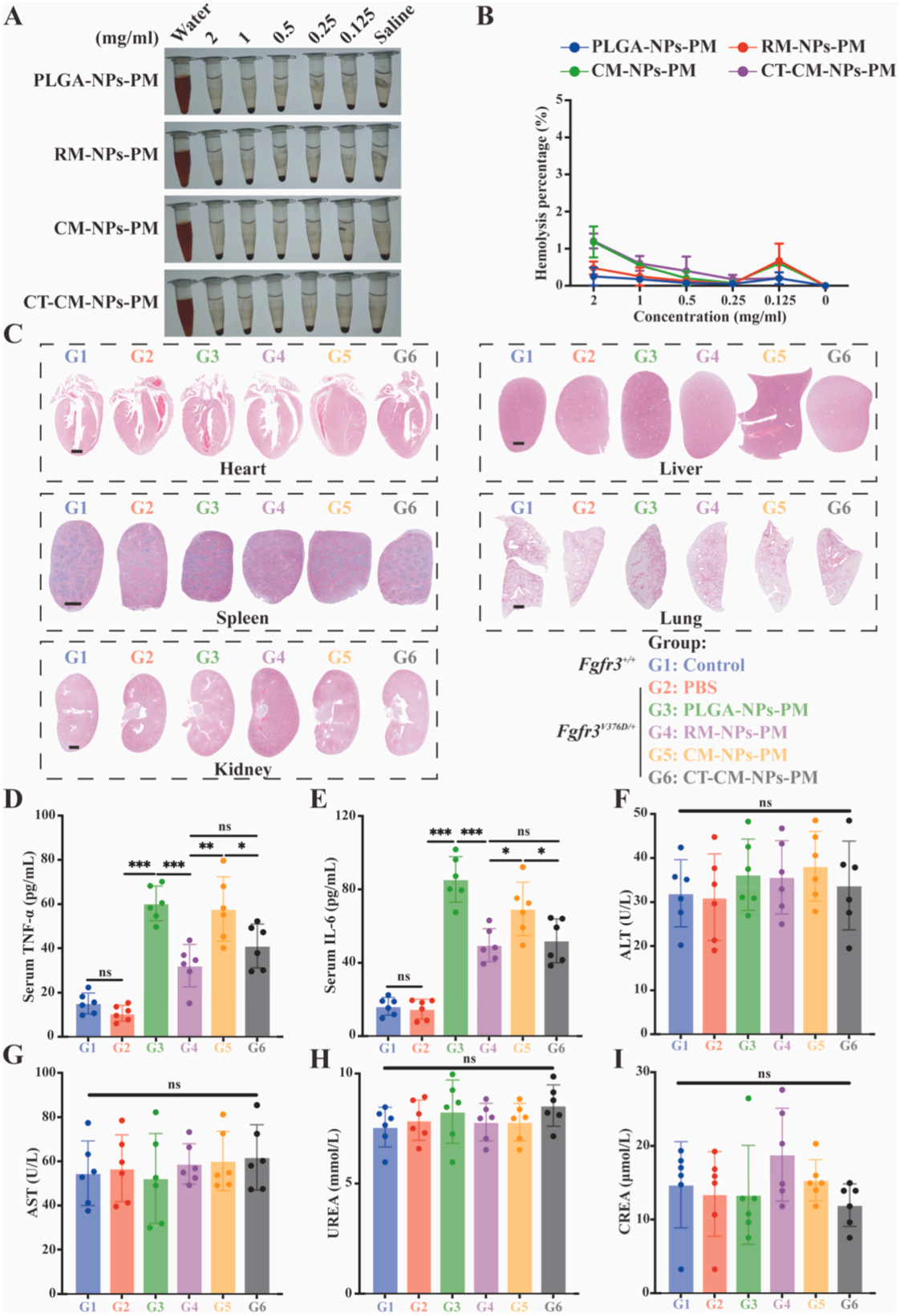

Fig. 9. In vivo biocompatibility of CT-CM-NPs-PM. (A) Representative hemolysis images following treatment with various nanoparticles at different concentrations. (B) Quantitative analysis of hemolysis degrees (n = 3). (C) H&E staining of major organs (heart, liver, spleen, lung, and kidney) from the indicated groups. Scale bars, 1 mm. (D and E) Proinflammatory cytokine levels of TNF-α and IL-6 in the serum of mice (n = 6). (F to I) ALT, AST, UREA and CREA levels after the indicated treatments (n = 6). Statistical analysis was performed using one-way ANOVA followed by Tukey's post-hoc test. Data are presented as mean ± SD, ns: not significant, $^{*}P < 0.05$, $^{**}P < 0.01$, and $^{***}P < 0.001$.

approved protocols by Xiamen University's Animal Care and Use Committee (XMULAC20210037).

CRediT authorship contribution statement

Shang-Hui Ye: Data curation, Formal analysis, Investigation, Methodology, Validation, Visualization, Writing – original draft. **Lian-Jie Li:** Data curation, Investigation, Supervision, Validation, Writing – review & editing. **Yi-Jiao Wang:** Data curation, Formal analysis, Supervision, Validation, Writing – review & editing. **Cheng-Run Yuan:** Data curation, Formal analysis, Validation, Visualization. **Jie Han:** Formal analysis, Software, Writing – review & editing. **Dan He:** Data curation, Formal analysis, Visualization. **Lin Che:** Data curation, Formal analysis, Validation. **Xiao-Hui Chen:** Data curation, Formal analysis, Methodology, Visualization. **Rong Shen:** Formal analysis, Project administration, Validation, Visualization. **Jian Yang:** Formal analysis, Methodology, Writing – review & editing. **Matthew B. Greenblatt:** Conceptualization, Methodology, Writing – review & editing. **Xian-Xian Yang:** Data curation, Funding acquisition, Resources. **Jian-Min Huang:** Funding acquisition, Project administration, Resources. **Jing Chen:** Conceptualization, Funding acquisition, Project administration, Writing – review & editing. **Ren Xu:** Conceptualization, Funding acquisition, Methodology, Project administration, Resources, Supervision, Writing – original draft, Writing – review & editing.

Declaration of competing interests

Jian Yang is an editor-in-chief for *Bioactive Materials* and was not involved in the editorial review or the decision to publish this article. All authors declare that there are no competing interests.

Acknowledgments

We appreciated all staff in our departments for the assistant in completing the work. Funding**:** This study was supported by the Major Program of National Natural Science Foundation of China (92468203), the National Natural Science Foundation of China (82372362, 82103859), Natural Science Foundation of Fujian Province (2022J06003, 2023J011602), the Scientific Research Foundation of State Key Laboratory of Vaccines for Infectious Diseases, Xiang An Biomedicine Laboratory (2023XAKJ0102051), Health and Medical Innovation Project of Fujian Province (2024CXB022), Health and Wellness High-Quality Development Science and Technology Program Medical Innovation Project of Xiamen (2024GZLCX23). **Notes:** During the preparation of this work the author(s) used ChatGPT 5.5 in order to polish the writing to meet the academic style. After using this tool/service, the author(s) reviewed and edited the content as needed and take(s) full responsibility for the content of the published article. **Competing interests:** The authors declare no conflict of interest.

Appendix A. Supplementary data

Supplementary data to this article can be found online at https://doi.org/10.1016/j.bioactmat.2026.06.018.

References

[1] P. Mertz, N. Costedoat-Chalumeau, M.A. Ferrada, G. Moulis, A. Mekinian, P. C. Grayson, L. Arnaud, Relapsing polychondritis: clinical updates and new differential diagnoses, Nat. Rev. Rheumatol. 20 (6) (2024) 347–360, https://doi.org/10.1038/s41584-024-01113-9.

[2] R. Savarirayan, J. Hoover-Fong, P. Yap, S.O. Fredwall, New treatments for children with achondroplasia, Lancet Child Adolesc. Health 8 (4) (2024) 301–310, https://doi.org/10.1016/s2352-4642(23)00310-3.

[3] Z. Jiang, S. Byers, M.L. Casal, L.J. Smith, Failures of endochondral ossification in the mucopolysaccharidoses, Curr. Osteoporos. Rep. 18 (6) (2020) 759–773, https://doi.org/10.1007/s11914-020-00626-y.

[4] J. Bertolin, V. Sánchez, A. Ribera, M.L. Jaén, M. Garcia, A. Pujol, X. Sánchez, S. Muñoz, S. Marcó, J. Pérez, et al., Treatment of skeletal and non-skeletal alterations of Mucopolysaccharidosis type IVA by AAV-mediated gene therapy, Nat. Commun. 12 (1) (2021) 5343, https://doi.org/10.1038/s41467-021-25697-y.

[5] B. Fafilek, M. Bosakova, P. Krejci, Expanding horizons of achondroplasia treatment: current options and future developments, Osteoarthr. Cartil. 30 (4) (2022) 535–544, https://doi.org/10.1016/j.joca.2021.11.017.

[6] S.R. Sangle, C.D. Hughes, L. Barry, S. Qureshi, C.K. Cheah, Y.J. Poh, D.P. D'Cruz, Relapsing polychondritis - a single Centre study in the United Kingdom, Autoimmun. Rev. 22 (8) (2023) 103352, https://doi.org/10.1016/j.autrev.2023.103352.

[7] A. Coi, M. Santoro, E. Garne, A. Pierini, M.C. Addor, J.L. Alessandri, J.E. H. Bergman, F. Bianchi, L. Boban, P. Braz, et al., Epidemiology of achondroplasia: a population-based study in Europe, Am. J. Med. Genet. 179 (9) (2019) 1791–1798, https://doi.org/10.1002/ajmg.a.61289.

[8] L. Loisay, D. Komla-Ebri, A. Morice, Y. Heuzé, C. Viaut, A. de La Seiglière, N. Kaci, D. Chan, A. Lamouroux, G. Baujat, et al., Hypochondroplasia gain-of-function mutation in FGFR3 causes defective bone mineralization in mice, JCI Insight 8 (12) (2023), https://doi.org/10.1172/jci.insight.168796.

[9] Y. Seino, Y. Yamanaka, M. Shinohara, S. Ikegami, M. Koike, M. Miyazawa, M. Inoue, T. Moriwake, H. Tanaka, Growth hormone therapy in achondroplasia, Horm. Res. 53 (Suppl 3) (2000) 53–56, https://doi.org/10.1159/000023534.

[10] H. Kanazawa, H. Tanaka, M. Inoue, Y. Yamanaka, N. Namba, Y. Seino, Efficacy of growth hormone therapy for patients with skeletal dysplasia, J. Bone Miner. Metabol. 21 (5) (2003) 307–310, https://doi.org/10.1007/s00774-003-0425-7.

[11] R. Sharma, J.J. Kopchick, V. Puri, V.M. Sharma, Effect of growth hormone on insulin signaling, Mol. Cell. Endocrinol. 518 (2020) 111038, https://doi.org/10.1016/j.mce.2020.111038.

[12] R. Savarirayan, J. Hoover-Fong, K. Ozono, P. Backeljauw, V. Cormier-Daire, K. DeAndrade, P. Ireland, M. Irving, J. Llerena Junior, M. Maghnie, et al., International consensus guidelines on the implementation and monitoring of vosoritide therapy in individuals with achondroplasia, Nat. Rev. Endocrinol. 21 (5) (2025) 314–324, https://doi.org/10.1038/s41574-024-01074-9.

[13] R. Savarirayan, L. Tofts, M. Irving, W.R. Wilcox, C.A. Bacino, J. Hoover-Fong, R. U. Font, P. Harmatz, F. Rutsch, M.B. Bober, et al., Safe and persistent growth-promoting effects of vosoritide in children with achondroplasia: 2-year results from an open-label, phase 3 extension study, Genet. Med. 23 (12) (2021) 2443–2447, https://doi.org/10.1038/s41436-021-01287-7.

[14] R. Savarirayan, W.R. Wilcox, P. Harmatz, J. Phillips 3rd, L.E. Polgreen, L. Tofts, K. Ozono, P. Arundel, M. Irving, C.A. Bacino, et al., Vosoritide therapy in children with achondroplasia aged 3-59 months: a multinational, randomised, double-blind, placebo-controlled, phase 2 trial, Lancet Child Adolesc. Health 8 (1) (2024) 40–50, https://doi.org/10.1016/s2352-4642(23)00265-1.

[15] L. Martin, N. Kaci, C. Benoist-Lasselin, M. Mondoloni, S. Decaudaveine, V. Estibals, M. Cornille, L. Loisay, J. Flipo, B. Demuynck, et al., Theobroma cacao improves bone growth by modulating defective ciliogenesis in a mouse model of achondroplasia, Bone Res. 10 (1) (2022) 8, https://doi.org/10.1038/s41413-021-00177-7.

[16] M. Kunova Bosakova, M. Varecha, M. Hampl, I. Duran, A. Nita, M. Buchtova, H. Dosedelova, R. Machat, Y. Xie, Z. Ni, et al., Regulation of ciliary function by fibroblast growth factor signaling identifies FGFR3-related disorders achondroplasia and thanatophoric dysplasia as ciliopathies, Hum. Mol. Genet. 27 (6) (2018) 1093–1105, https://doi.org/10.1093/hmg/ddy031.

[17] R.H. Fang, W. Gao, L. Zhang, Targeting drugs to tumours using cell membrane-coated nanoparticles, Nat. Rev. Clin. Oncol. 20 (1) (2023) 33–48, https://doi.org/10.1038/s41571-022-00699-x.

[18] I. Ferreira-Faria, S. Yousefiasl, A. Macário-Soares, M. Pereira-Silva, D. Peixoto, H. Zafar, F. Raza, H. Faneca, F. Veiga, M.R. Hamblin, et al., Stem cell membrane-coated abiotic nanomaterials for biomedical applications, J. Contr. Release 351 (2022) 174–197, https://doi.org/10.1016/j.jconrel.2022.09.012.

[19] C. Jiang, X. Yang, Q. Huang, T. Lei, H. Luo, D. Wu, Z. Yang, Y. Xu, Y. Dou, X. Ma, et al., Microglial-biomimetic memantine-loaded polydopamine nanomedicines for alleviating depression, Adv. Mater. 37 (9) (2025) e2417869, https://doi.org/10.1002/adma.202417869.

[20] S. Chen, D. Tian, X. Yang, Q. Yin, L. Li, Y. Lin, S. Liu, H. Chen, M. Zhang, J. Lin, et al., Biocompatible assessment of erythrocyte membrane-camouflaged polymeric PLGA nanoparticles in pregnant mice: both on maternal and fetal/juvenile mice, Int. J. Nanomed. 17 (2022) 5899–5913, https://doi.org/10.2147/ijn.S384906.

[21] Z. Guo, S. Gao, Z. Wang, Z. Chen, J. Chen, A. Duan, F. Xu, Q. Wang, W. Qin, C. Zeng, et al., Engineered RGD-Treg-Exos targeted delivery of miR-218-5p to activate mitophagy and attenuate podocyte injury in diabetic kidney disease, Adv. Sci. (Weinh.) 12 (37) (2025) e12034, https://doi.org/10.1002/advs.202412034.

[22] J. Zhang, C. Ji, H. Zhang, H. Shi, F. Mao, H. Qian, W. Xu, D. Wang, J. Pan, X. Fang, et al., Engineered neutrophil-derived exosome-like vesicles for targeted cancer therapy, Sci. Adv. 8 (2) (2022), https://doi.org/10.1126/sciadv.abj8207 eabj8207.

[23] Y. Yu, Q. Cheng, X. Ji, H. Chen, W. Zeng, X. Zeng, Y. Zhao, L. Mei, Engineered drug-loaded cellular membrane nanovesicles for efficient treatment of postsurgical cancer recurrence and metastasis, Sci. Adv. 8 (49) (2022), https://doi.org/10.1126/sciadv.add3599 eadd3599.

[24] Y. Liu, J. Ren, W. Zhang, L. Ding, R. Ma, M. Zhang, S. Zheng, R. Liang, Y. Zhang, Astroglial membrane camouflaged Ptbp1 siRNA delivery hinders glutamate homeostasis via SDH/Nrf2 pathway, Biomaterials 312 (2025) 122707, https://doi.org/10.1016/j.biomaterials.2024.122707.

[25] P.H. Lin, C. Huang, Y. Hu, V.S. Ramanujam, E.S. Lee, R. Singh, U. Milbreta, C. Cheung, J.Y. Ying, S.Y. Chew, Neural cell membrane-coated DNA nanogels as a potential target-specific drug delivery tool for the central nervous system,

Biomaterials 302 (2023) 122325, https://doi.org/10.1016/j.biomaterials.2023.122325.
[26] D. Wang, S. Lin, T. Li, X. Yang, X. Zhong, Q. Chen, G. Jiang, C. Li, Cancer cell membrane-coated siRNA-Decorated Au/MnO(2) nanosensitizers for synergistically enhanced radio-immunotherapy of breast cancer, Mater. Today Bio 29 (2024) 101275, https://doi.org/10.1016/j.mtbio.2024.101275.
[27] R. Deng, R. Zhao, Z. Zhang, Y. Chen, M. Yang, Y. Lin, J. Ye, N. Li, H. Qin, X. Yan, et al., Chondrocyte membrane-coated nanoparticles promote drug retention and halt cartilage damage in rat and canine osteoarthritis, Sci. Transl. Med. 16 (735) (2024), https://doi.org/10.1126/scitranslmed.adh9751 eadh9751.
[28] P. Chen, X. Liu, C. Gu, P. Zhong, N. Song, M. Li, Z. Dai, X. Fang, Z. Liu, J. Zhang, et al., A plant-derived natural photosynthetic system for improving cell anabolism, Nature 612 (7940) (2022) 546–554, https://doi.org/10.1038/s41586-022-05499-y.
[29] D.A. Rothenfluh, H. Bermudez, C.P. O'Neil, J.A. Hubbell, Biofunctional polymer nanoparticles for intra-articular targeting and retention in cartilage, Nat. Mater. 7 (3) (2008) 248–254, https://doi.org/10.1038/nmat2116.
[30] D. Zhao, Y. Li, L. Xiang, Q. Saiding, Z. Lin, Z. Cai, J. Wang, W. Cui, Cell shock absorption via stress relaxation hydrogel microspheres for alleviating endoplasmic reticulum stress in chondrocytes, Research 8 (2025) 777, https://doi.org/10.34133/research.0777.
[31] J. Chen, D. He, C. Yuan, N. Li, B. Shi, C. Niu, J. Yang, L. Zheng, L. Che, R. Xu, Fibroblast growth factor receptor 3 mutation promotes HSPB6-mediated cuproptosis in hypochondroplasia by impairing chondrocyte autophagy, J. Orthop. Transl. 51 (2025) 68–81, https://doi.org/10.1016/j.jot.2025.01.011.
[32] C. Liu, X. Liu, X. Xiang, X. Pang, S. Chen, Y. Zhang, E. Ren, L. Zhang, X. Liu, P. Lv, et al., A nanovaccine for antigen self-presentation and immunosuppression reversal as a personalized cancer immunotherapy strategy, Nat. Nanotechnol. 17 (5) (2022) 531–540, https://doi.org/10.1038/s41565-022-01098-0.
[33] C.L. Xie, S.H. Ye, Y.T. Yue, B.H. Shi, J.P. Xu, L.J. Li, Z.B. Zou, M.B. Greenblatt, N. Li, X.W. Yang, et al., Viridicatol from the deep-sea-derived fungus alleviates bone loss by targeting the Wnt/SHN3 pathway, Adv. Sci. (Weinh.) (2025) e2416140, https://doi.org/10.1002/advs.202416140.
[34] R. Xu, A. Yallowitz, A. Qin, Z. Wu, D.Y. Shin, J.M. Kim, S. Debnath, G. Ji, M. P. Bostrom, X. Yang, et al., Targeting skeletal endothelium to ameliorate bone loss, Nat. Med. 24 (6) (2018) 823–833, https://doi.org/10.1038/s41591-018-0020-z.
[35] L. Chen, J. Yang, Z. Cai, Y. Huang, P. Xiao, H. Chen, X. Luo, W. Huang, W. Cui, N. Hu, Mitochondrial-oriented injectable hydrogel microspheres maintain homeostasis of chondrocyte metabolism to promote subcellular therapy in osteoarthritis, Research 7 (2024) 306, https://doi.org/10.34133/research.0306.
[36] K. Feng, J. Liu, L. Gong, T. Ye, Z. Chen, Y. Wang, Q. Li, X. Xie, Engineered MSC-sEVs as a versatile nanoplatform for enhanced osteoarthritis treatment via targeted elimination of senescent chondrocytes and maintenance of cartilage matrix metabolic homeostasis, Adv. Sci. (Weinh.) 12 (8) (2025) e2413759, https://doi.org/10.1002/advs.202413759.
[37] S. Sinha, J.K. Chen, Purmorphamine activates the hedgehog pathway by targeting smoothened, Nat. Chem. Biol. 2 (1) (2006) 29–30, https://doi.org/10.1038/nchembio753.
[38] C.S. Lee, S. Kim, J. Fan, H.S. Hwang, T. Aghaloo, M. Lee, Smoothened agonist sterosome immobilized hybrid scaffold for bone regeneration, Sci. Adv. 6 (17) (2020), https://doi.org/10.1126/sciadv.aaz7822 eaaz7822.
[39] J. Chen, J. Yang, S. Zhao, H. Ying, G. Li, C. Xu, Identification of a novel mutation in the FGFR3 gene in a Chinese family with Hypochondroplasia, Gene 641 (2018) 355–360, https://doi.org/10.1016/j.gene.2017.10.062.
[40] Q. Lu, T. Liu, Z. Han, J. Zhao, X. Fan, H. Wang, J. Song, H. Ye, J. Sun, Revolutionizing cancer treatment: the power of cell-based drug delivery systems, J. Contr. Release 361 (2023) 604–620, https://doi.org/10.1016/j.jconrel.2023.08.023.
[41] C. Geng, X. Ren, P. Cao, X. Chu, P. Wei, Q. Liu, Y. Lu, B. Fu, W. Li, Y. Li, et al., Macrophage membrane–biomimetic nanoparticles target inflammatory microenvironment for epilepsy treatment, Theranostics 14 (17) (2024) 6652–6670, https://doi.org/10.7150/thno.99260.
[42] K. Qin, F. Meng, D. Han, W. Guo, X. Li, Z. Li, L. Du, H. Zhou, H. Yan, Y. Peng, et al., Enzyme-armed nanocleaner provides superior detoxification against organophosphorus compounds via a dual-action mechanism, J. Nanobiotechnol. 22 (1) (2024) 593, https://doi.org/10.1186/s12951-024-02869-8.
[43] Q. Yang, J. Liu, Y. Liu, S. Liu, X. Wei, Y. Yang, W. Zhang, S. Zhang, M. Zhang, B. Liu, et al., A biomimetic multimodal nanoplatform combining neutrophil-coated two-dimensional metalloporphyrinic framework nanosheet and exendin-4 to treat obesity-related osteoporosis, Mater. Today Bio 33 (2025) 102009, https://doi.org/10.1016/j.mtbio.2025.102009.
[44] W. Knudson, S. Ishizuka, K. Terabe, E.B. Askew, C.B. Knudson, The pericellular hyaluronan of articular chondrocytes, Matrix Biol. 78–79 (2019) 32–46, https://doi.org/10.1016/j.matbio.2018.02.005.
[45] R.F. Loeser, Integrins and chondrocyte-matrix interactions in articular cartilage, Matrix Biol. 39 (2014) 11–16, https://doi.org/10.1016/j.matbio.2014.08.007.
[46] E. Mitsou, J. Klein, Liposome-based interventions in knee osteoarthritis, Small 21 (17) (2025) e2410060, https://doi.org/10.1002/smll.202410060.
[47] Y. Chen, M. Zhu, B. Huang, Y. Jiang, J. Su, Advances in cell membrane-coated nanoparticles and their applications for bone therapy, Biomater. Adv. 144 (2023) 213232, https://doi.org/10.1016/j.bioadv.2022.213232.
[48] X. Wei, J. Qiu, R. Lai, T. Wei, Z. Lin, S. Huang, Y. Jiang, Z. Kuang, H. Zeng, Y. Gong, et al., A human organoid drug screen identifies α2-adrenergic receptor signaling as a therapeutic target for cartilage regeneration, Cell Stem Cell 31 (12) (2024) 1813–1830.e1818, https://doi.org/10.1016/j.stem.2024.09.001.